TOMBALL TECHNOLOGY CENTER

Geomechanics

BJS – NE REGION
ELASTIC PROPERTIES AND FORMATION HARDNESS TESTING OF BIG LIME FORMATION CORE BEFORE AND AFTER EXPOSURE TO 15% HCL AND FOAMED ACIDS

TECHNOLOGY CENTER REPORT NO. 06-10-0906RM

BJ SERVICES TECHNICAL REPRESENTATIVE:

MR. ROGER MYERS

PITTSBURGH, PENNSYLVANIA

MARCH 6, 2007

EXECUTIVE SUMMARY

Young's modulus and Poisson's Ratio were measured in Big Lime formation cores from the Charleston East field. Both ultrasonic and static test methods were employed. All tests were conducted under triaxial test conditions on dry cores at room temperature. In addition, the formation hardness on a single core plug was measured before and after exposure to HCl and foamed acids.

Results indicated that the exposure to 15% HCl for up to nine minutes reduced the surface hardness only slightly and exposure to a foamed acid after 24 minutes produces no change in formation hardness.

The static Young's modulus varied from 3.94×10^6 psi to 8.55×10^6 psi. The static Poisson's Ratio varied from 0.11 to 0.22. The static Young's modulus correlated well with bulk density, porosity, p-wave and s-wave transit times, and the dynamic Young's modulus. The static Poisson's Ratio correlated only weakly to bulk density. The average ratio of static to dynamic Poisson's Ratio was 0.60. The average ratio of static to dynamic Poisson's Ratio was 0.72. The p-wave and s-wave transit times were affected most by porosity (and bulk density) and very little by the average grain density. The transit times were very fast and approached the values in pure calcite (T_p = 47.6 μsec/ft and T_s = 91 μsec/ft) in the low porosity cores. A very good positive correlation existed between the p-wave and s-wave transit times.

INTRODUCTION

This report contains the test results of the mechanical property measurements on Big Lime formation core plugs from the West Virginia GES core library. This work was part of a larger effort to evaluate stimulation options, especially in the area of acid fracturing. Geological, mineralogical and acid core flow studies were completed and reported[1],[2]. This report focuses on the measurements of the elastic properties of the Big Lime. Specifically, Young's modulus and Poisson's Ratio were measured. These constants are required input into commercial hydraulic fracture models and triaxial testing on core is considered by many in the industry the best way to determine these constants.

In addition to mechanical properties, formation hardness on a single core plug was measured before and after exposure to 15% HCl and foamed acids. These tests were performed to determine whether significant softening or mechanical "damage" occurred that might lead to the loss of fracture conductivity under anticipated drawdown pressures.

Cross-plots between static and dynamic elastic constants, porosity, bulk density, and ultrasonic transit times are presented to assist in efforts to calibrate wireline logs and/or generate synthetic mechanical property logs.

SAMPLE DESCRIPTIONS

One-inch diameter core plugs were drilled from wholecore sections from the Hardy #14 well situated in the Charleston East field in Kanahwa County, West Virginia. An inventory of the core plugs along with some physical properties is presented in Table 1. XRD analysis[1] indicated that calcite and Fe-dolomite were the primary mineral components. All core plugs were drilled perpendicular to the whole core axis.

Table 1
Inventory of Big Lime Core Plugs

Sample	Depth (ft)	Length (in.)	Diameter (in.)	Dry Bulk Density (g/cc)	Porosity* (%)	Air* Permeability (mD)	Grain Density* (g/cc)
C	1387.50	1.951	0.997	2.609	3.6	0.02	2.719
F	1388.10	1.939	0.997	2.740	1.7	0.02	2.778
L	1391.20	1.955	0.997	2.529	8.4	0.03	2.760
N	1391.30	1.953	0.997	2.443	12.5	0.05	2.784
V	1393.20	1.938	0.997	2.658	5.6	0.03	2.806
Y	1393.75	1.955	0.998	2.679	3.6	0.02	2.782
CC	1394.10	1.933	0.998	2.706	2.5	0.02	2.776
GG	1394.60	1.934	0.998	2.562	9.8	0.05	2.844
KK	1395.00	1.930	0.998	2.546	11.2	0.28	2.866
UU	1397.50	1.943	0.998	2.453	13.2	0.44	2.832
WW	1402.30	1.925	0.997	2.656	5.7	0.02	2.825
YY	1402.65	1.942	0.998	2.710	6.0	0.02	2.887

* see BJS TTC Report[1]

SPECIAL ACID SOLUBILITY REACTION TIME TEST

Initial tests were conducted on a core sample taken from a depth of 1387.75 feet. A portion of this core specimen was broken into three sections. Each section was weighed and the approximate volume of 15 % HCl required to dissolve 65 % (assuming 100 % Calcite) of the total section was calculated. Three test fluids of 15 % HCl containing 1 gpt of CI-14 CORROSION INHIBITOR and other additives listed below were used to test each section. Each section was placed into the test acid at 72^{o}F for 15 minutes. Each section was removed from the acid, washed and dried. The final weight of each section was determined and the actual solubility of each section was calculated. The results, displayed in the Table 2, demonstrate that the foamed acid system (fluid system B) provided more retardation than acid test fluids A or C.

Table 2
Results of Acid Solubility Tests

Test Acid	Initial Weight (Grams)	Final Weight (Grams)	Percent Solubility (based on available Acid) in 15 minutes at 72 ^{o}F
15 % HCl + 1 gpt CI-14	30.3451	14.3707	80
15 % HCl + 1 gpt CI-14 + 5gpt FAW-21	23.9002	15.6215	51
15 % HCl + 1 gpt CI-14 + 4gpt SLA-48	19.5588	9.0664	82

SURFACE EXPOSURE FLUIDS

One face of Sample KK was exposed to a 15% HCl acid at room temperature for 3 minutes, after which the formation hardness was measured. The same surface was then exposed for an additional 3 minutes and the formation hardness was re-measured. This was followed by an additional 3 minute exposure and formation hardness measurement.

The surface of Sample KK was then smoothed to allow for a new test using a foamed acid formulation. The surface was treated at room temperature for 24 minutes after which the formation hardness was measured. Photographs of the surface before and after acid exposure are located in Appendix III.

RESULTS AND INTERPRETATION

Formation Hardness Testing

Table 3 displays formation hardness of sample KK before and after exposure to 15% HCl and foamed acids. Note that there was not a large reduction in hardness after exposure to the HCl, and no change in hardness after exposure to the foamed acid. Photographs in Appendix III show a much coarser surface using HCl compared to foamed acid.

The HCl treated surface shows individual quartz grains that remained after removal of the carbonate. This texture seems to provide a natural mechanism for differential etching. This suggests that parts of the formation containing large quartz grains might be a good candidate for acid fracturing.

Table 3
Effect of Acid Treatment on Formation Hardness (kg/mm^2) – Sample KK

		15% HCl					Foamed Acid
	Pre-soak	**3 min.**	**6 min.**	**9 min.**		**Pre-Soak**	**24 min.**
ave.	84.7	78.0	62.0	74.5		97	92.4
stdev.	8	5.0	8.6	15.4		4	3.1

Dynamic Elastic Properties

The dynamic elastic properties were measured using a standard through-transmission pulsed ultrasonic technique. Details of the test procedures are discussed in the next section. In short, the dynamic elastic moduli (Young's modulus and Poisson's Ratio) were calculated from measurements of the compressional and shear wave velocities and bulk density using Equations (5) and (6). The wave velocities were first measured as a function of net mean stress. Linear least-square regressions of wave velocity versus stress were then performed on each data set. The coefficients of each regression were used to calculate the wave velocities and dynamic elastic moduli at the reservoir net mean stress. The dynamic and static elastic properties of Sample KK were measured prior to the acid exposures.

The reservoir net mean stress was estimated from assumed by typical values of overburden stress, closure stress, and reservoir pressure gradients of 1 psi/ft and 0.7 psi/ft, and 0.45 psi/ft, respectively. The reservoir net mean stress was calculated from the expression:

$$\sigma'_m = [(G_o + 2G_c)/3 - \alpha G_p]D \qquad (1)$$

The letter "G" represents the gradient. α is the poro-elastic constant, and was assumed equal to 0.8. D is depth (in feet), and the subscripts, o, c, p, and m, represent the overburden, closure, reservoir pressure, and mean stress, respectively. Core depths ranged from 1387 feet to 1402 feet. As a result, the reservoir net mean stress ranged from 611 psi to 617 psi.

The results of the ultrasonic wave velocity measurements and the derived elastic constants are listed in Table 4. The inverse wave velocities or transit times are listed in the table and expressed in units of microseconds per foot (μsec/ft).

Static Elastic Properties

The static Young's modulus and Poisson's Ratio were measured following test procedures discussed in the next section and measured concurrently with the dynamic elastic properties. In short, all tests were conducted on room dried core at room temperature (~72 ^{o}F) and with a confining stress equal to 2000 psi. Each sample was stress cycled twice to eliminate the effect of stress hysteresis on the strain measurements. Young's modulus and Poisson's Ratio were determined along the increasing axial stress path of the second cycle. The results are summarized in Table 5. The stress-strain curves from which the elastic constants were determined are located in Appendix II.

Static/Dynamic Correlations

This section presents analyses using data presented in Tables 1, 4 and 5 that attempts to reveal empirical relations between various quantities that may assist in estimating the static moduli from more commonly acquired wireline log data and in calibrating current wireline-derived mechanical property logs. The relations discussed in this section are meant to serve only as a guide for identifying those quantities that might correlate strongly with the static and dynamic elastic moduli.

Figures 1 and 2 display cross-plots of the static Young's modulus and Poisson's Ratio versus the bulk density of the cores. The trends are not strong, but do suggest that these two elastic constants tend to increase with increasing bulk density. Bulk density is a function of mineralogy (as reflected by grain density) and porosity via the relation:

$$\rho_b = \rho_g(1 - \phi) + \rho_f\phi \qquad (2)$$

ρ_b is the bulk density, ρ_g is the average density of the solid phase (i.e. grain density), ρ_f is pore fluid density, and ϕ is porosity. Because the samples were tested dry, the fluid density was essentially zero. Equation (2) shows that changes in bulk density in dry core result from the combined effect of changes in grain density and/or porosity.

Reductions in Young's modulus with increasing porosity are to be expected because adding void space to a solid usually reduces its stiffness. The effect of porosity on Poisson's Ratio is less certain. A cross-plot of static Young's modulus versus grain density (not shown) showed a weak negative trend (i.e. decreasing modulus with increasing grain density). However, no trend was observed between grain density and the static Poisson's Ratio.

Figure 3 shows a strong negative correlation, as expected, between the static (and dynamic) Young's modulus and porosity. Figure 4 shows no correlation between porosity and the static Poisson's Ratio, and only a weak negative correlation with the dynamic Poisson's Ratio.

Figure 5 displays cross-plots of the s-wave and p-wave transit times versus porosity. This figure indicates very strong correlation of increasing transit time with increasing porosity. There were also trends (not shown) showing decreasing transit times with increasing bulk density, but no trends of transit times versus grain density.

As for the correlation between static and dynamic elastic properties, Figure 6 displays cross-plots of the static Young's modulus versus p-wave and s-wave transit times. Good power-law fits resulted from the regression analysis. Little to no correlation was observed between the transit times and static Poisson's Ratio (not shown). Figure 7 displays a good positive correlation between static and dynamic Young's modulus. Figure 8 shows that no correlation appears to exist between the static and dynamic Poisson's Ratio. Figure 8 does indicate that the dynamic values are systematically greater than the static values. The average ratio of static to dynamic Poisson's Ratio (from Table 4) was 0.60.

$$\nu_s/\nu_{dyn} = 0.60 \qquad (3)$$

Also, the average ratio of static to dynamic Young's modulus was:

$$E_s/E_{dyn} = 0.72 \qquad (4)$$

This is a remarkably good agreement among limestone moduli considering that most sandstone and shale rock types display ratios between 0.6 to 0.4.

Finally, Figure 9 displays a cross-plot of the s-wave versus p-wave transit times. The correlation is very good and suggests that s-wave transit times should be able to be deduced from p-wave transit times with relative accuracy. This would be especially important in wells lacking the s-wave component in a density-sonic log suite.

In summary, the exposure to 15% HCl for up to nine minutes reduced the surface hardness only slightly and exposure to a foamed acid after 24 minutes produces no change in formation hardness. The p-wave and s-wave transit times were affected most by porosity (and bulk density) and very little by the average grain density. The transit times were very fast and approached the values in pure calcite (T_p = 47.6 μsec/ft and T_s = 91 μsec/ft) in the low porosity cores. A very good positive correlation existed between the p-wave and s-wave transit times. The static Young's modulus varied from $3.94x10^6$ psi to $8.55x10^6$ psi. The static Poisson's Ratio varied from 0.11 to 0.22. The static Young's modulus correlated well with bulk density, porosity, p-wave and s-wave transit times, and the dynamic Young's modulus. The static Poisson's Ratio correlated only weakly to bulk density. The average ratio of static to dynamic Poisson's Ratio was 0.60. The average ratio of static to dynamic Poisson's Ratio was 0.72.

Table 4
Dynamic Elastic Properties of Big Lime Core Samples

Sample	Depth (ft)	Net Mean Stress (psi)	Poisson's Ratio	Young's Modulus ($x10^6$ psi)	P-wave Transit Time (μsec/ft)	S-wave Transit Time (μsec/ft)
C	1387.50	611	0.305	8.76	54.2	102.4
F	1388.10	611	0.281	10.1	53.5	96.8
L	1391.20	612	0.240	7.44	62.3	106.5
N	1391.30	612	0.246	6.66	64.4	110.9
V	1393.20	613	0.271	9.33	55.4	98.8
Y	1393.75	613	0.263	10.3	53.4	94.2
CC	1394.10	613	0.282	10.4	52.1	94.6
GG	1394.60	614	0.259	8.53	59.5	104.4
KK	1395.00	614	0.266	7.27	61.7	109.3
UU	1397.50	615	0.261	6.02	66.9	117.6
WW	1402.30	617	0.296	9.03	54.6	101.3
YY	1402.65	617	0.309	8.80	54.8	104.2

Table 5
Static Elastic Properties of Big Lime Core Samples

Sample	Depth (ft)	Poisson's Ratio	Young's Modulus ($x10^6$ psi)	ν_s/ν_{dyn}	E_s/E_{dyn}
C	1387.5	0.221	7.41	0.724	0.846
F	1388.1	0.153	7.82	0.545	0.775
L	1391.2	0.171	6.03	0.714	0.810
N	1391.3	0.118	4.82	0.479	0.698
V	1393.2	0.115	6.03	0.424	0.646
Y	1393.75	0.148	8.55	0.562	0.832
CC	1394.1	0.137	7.40	0.485	0.709
GG	1394.6	0.201	6.07	0.775	0.711
KK	1395.0	0.164	4.58	0.616	0.630
UU	1397.5	0.204	3.94	0.781	0.654
WW	1402.3	0.181	6.90	0.612	0.764
YY	1402.65	0.151	5.07	0.488	0.576

Figure 1
Static Young's Modulus versus Bulk Density

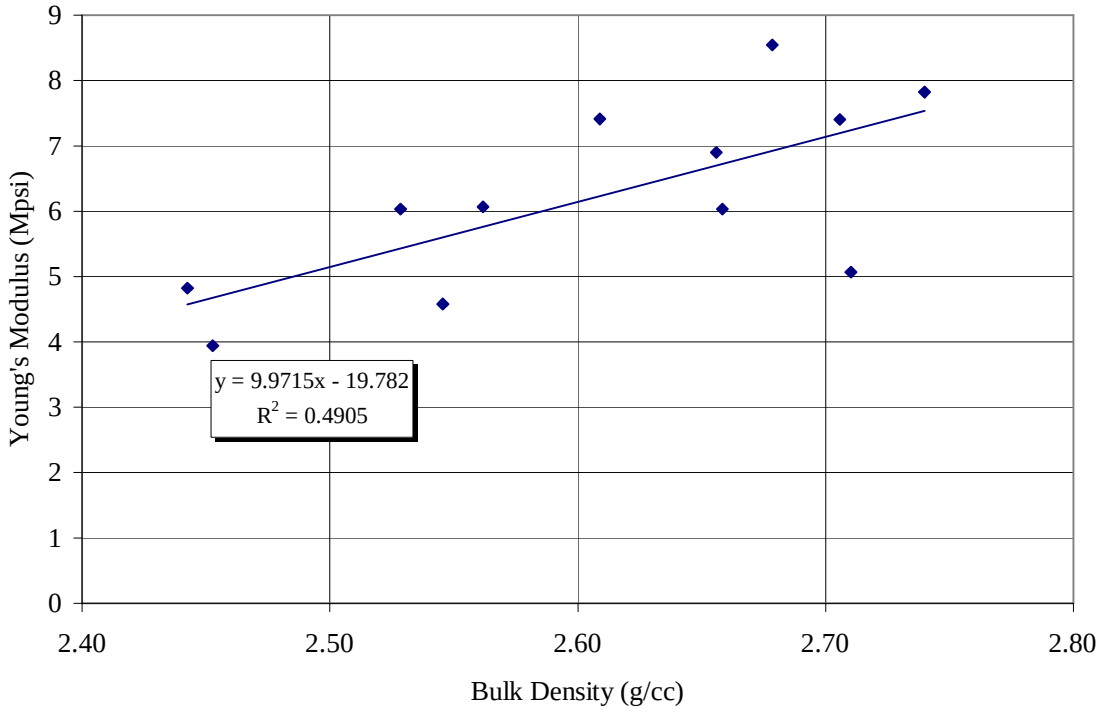

Figure 2
Static Poisson's Ratio versus Bulk Density

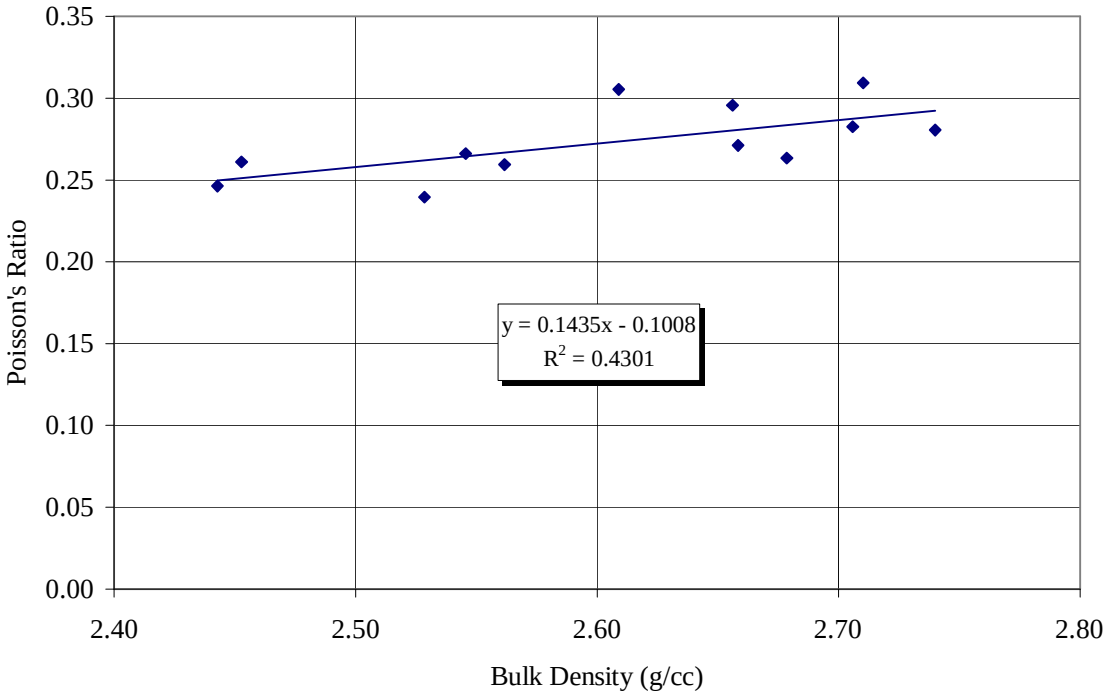

Figure 3
Static and Dynamic Young's Modulus versus Porosity

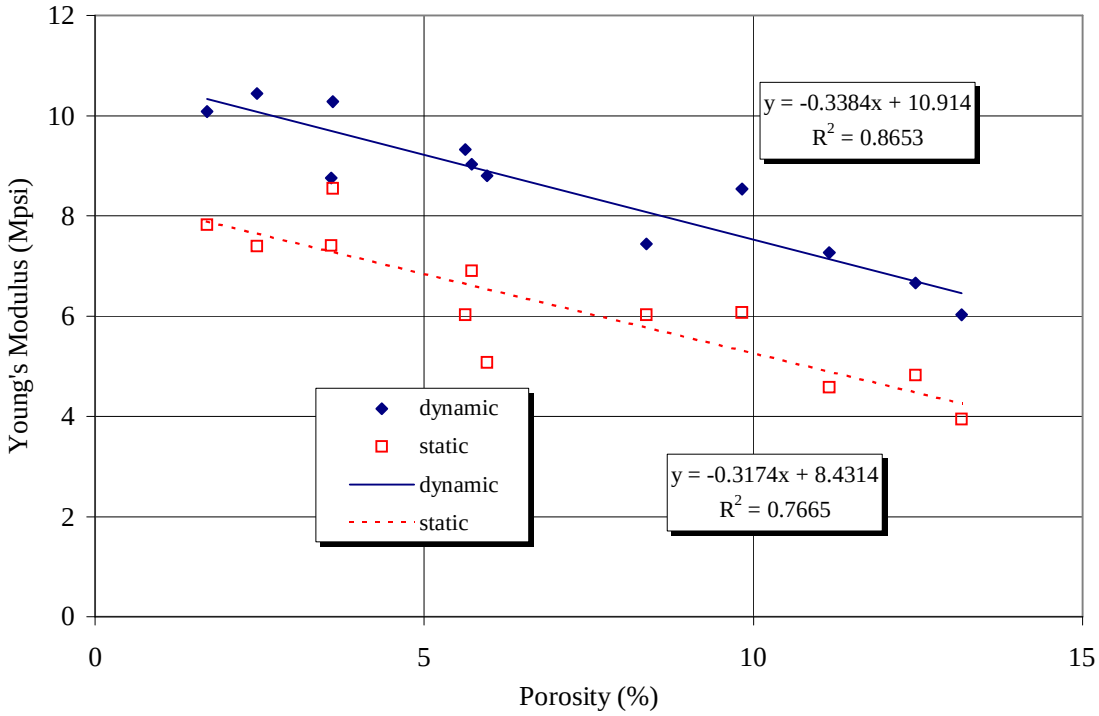

Figure 4
Static and Dynamic Poisson's Ratio versus Porosity

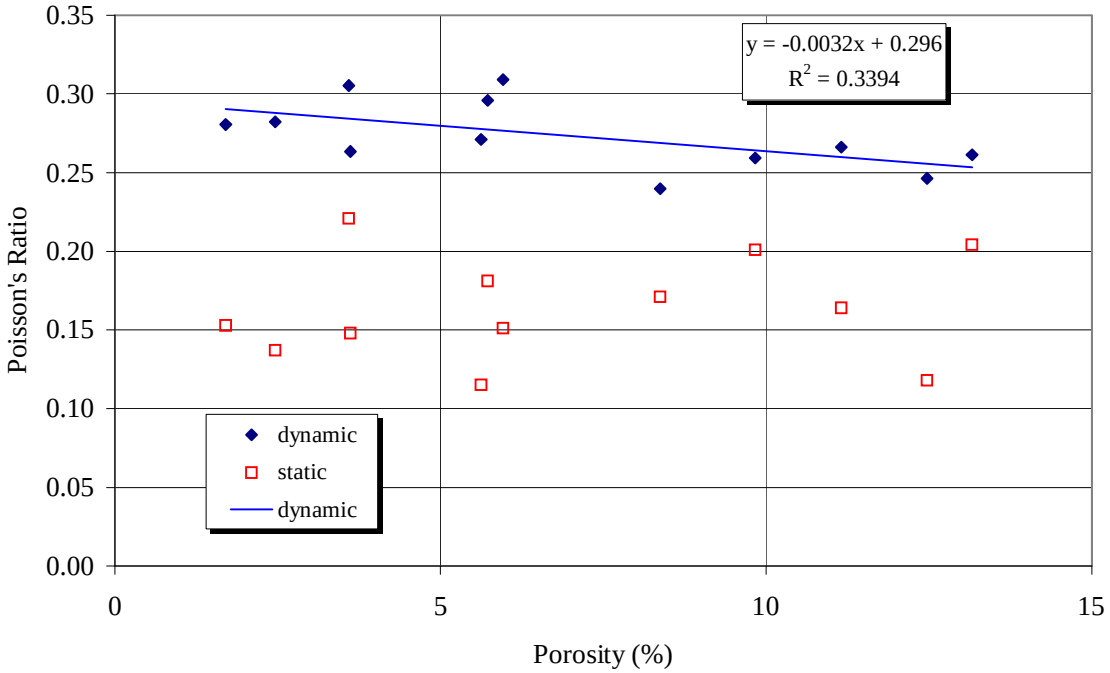

Figure 5
Ultrasonic Wave Transit Times versus Porosity

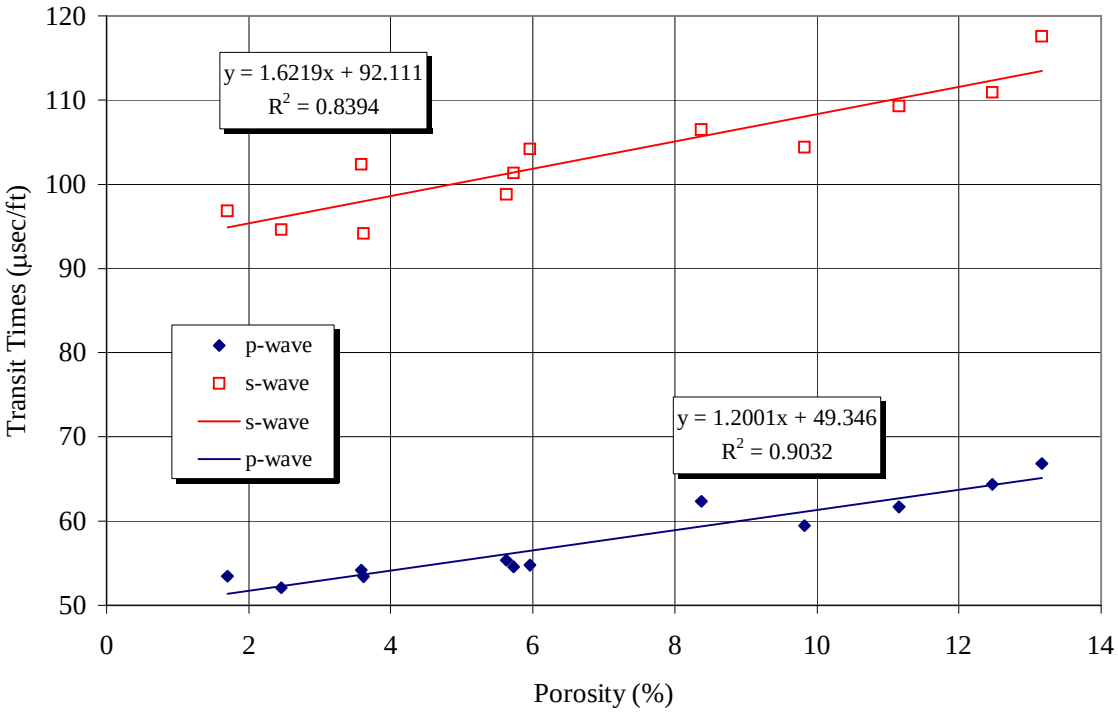

Figure 6
Static Young's Modulus versus Ultrasonic Transit Times

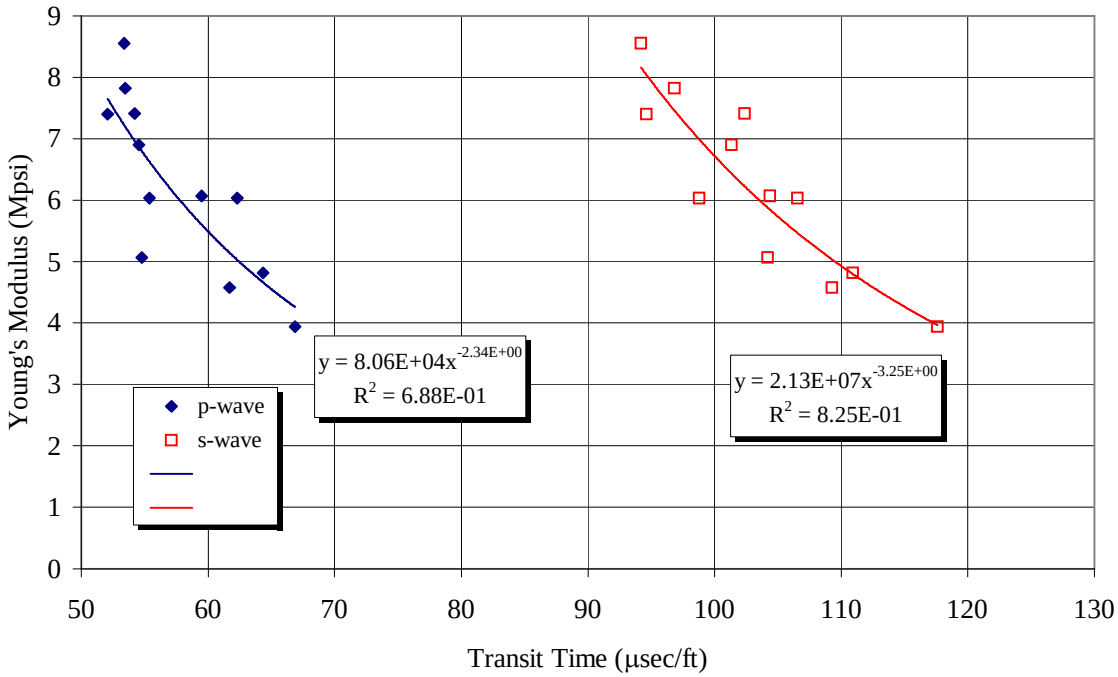

Figure 7
Static versus Dynamic Young's Modulus

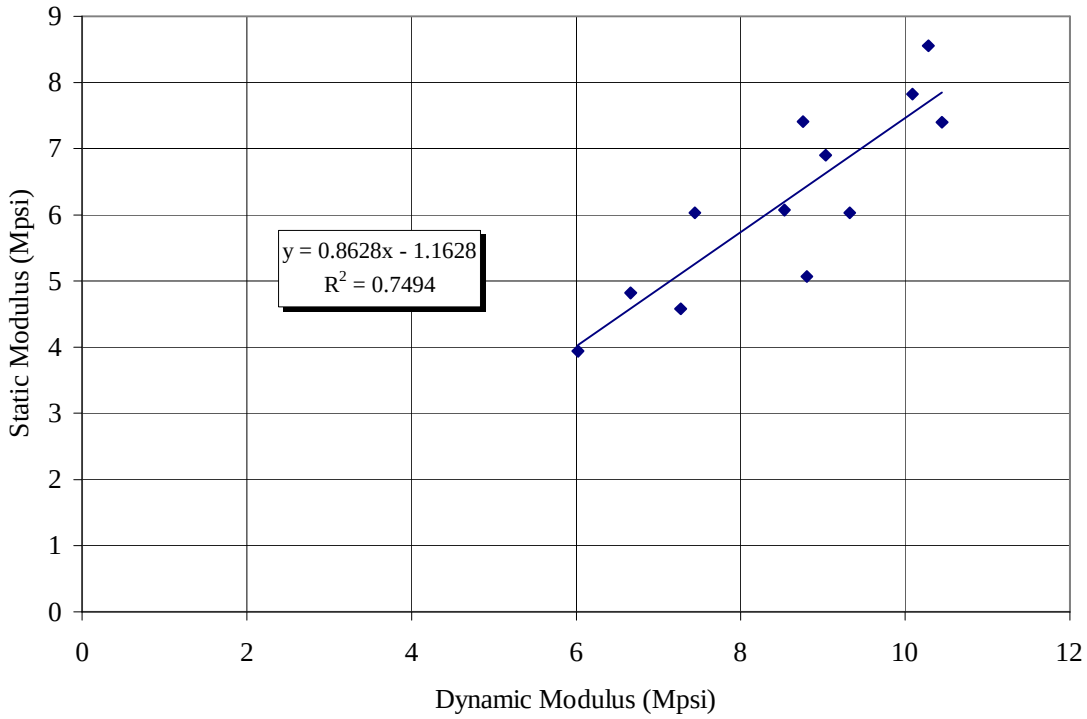

Figure 8
Static versus Dynamic Poisson's Ratio

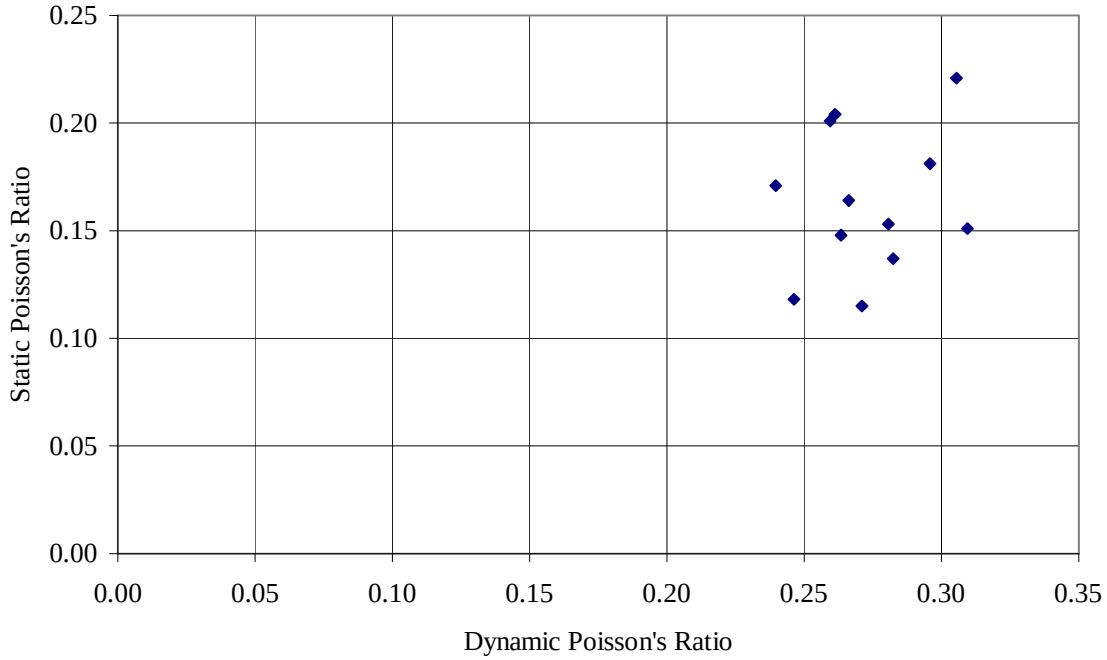

Figure 9
Shear Wave versus Compressional Wave Transit Tiimes

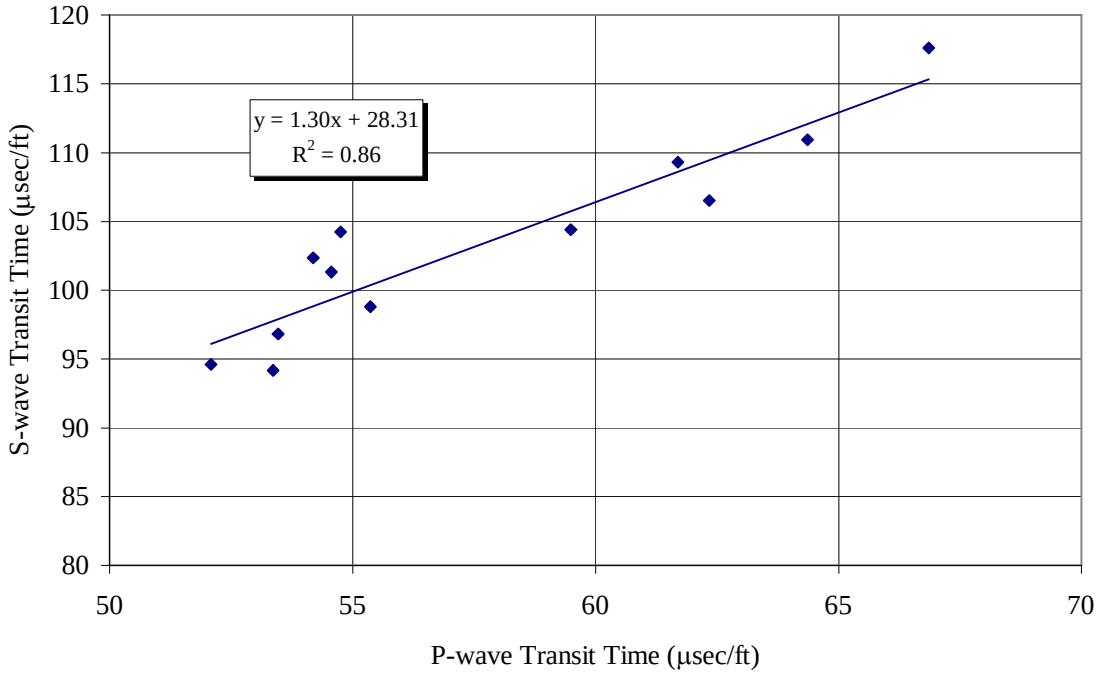

TEST PROCEDURES

Dynamic Elastic Properties

Plugs were drilled using a light oil called Isopar. One-inch diameter cylindrical samples were prepared by grinding the surfaces parallel and smooth to within a tolerance of 0.001 inch. Cores were drilled in directions perpendicular to the whole core axis. Core plugs were then "cleaned" of pore fluids, dried and measured for porosity and air permeability. The core plugs were then ready for mechanical property measurements.

The dynamic elastic properties of each sample were determined by measuring the ultrasonic compressional and shear wave velocities as a function of stress using a standard pulsed through-transmission method. Each sample was first loaded hydrostatically to a confining stress of 2000 psi. The polarized shear-wave signal was then digitally recorded. The axial stress was then increased an additional 3800 psi and the s-wave signal recorded again. The axial stress was then unloaded back to the confining stress and the axial stress cycle repeated. The s-wave signals were recorded at the extreme axial load points. The p-wave signal was inferred from the mode-converted shear wave signal. The polarization direction of the shear wave was set up to propagate perpendicular to the bedding planes of the horizontally cut cores. The bedding planes were difficult to see and exact alignment with the plane of polarization may not have been achieved.

The transmitting transducers were energized using a high voltage spike pulser (900-volt max.). Both the shear wave and compressional wave signals were amplified, band-pass filtered, and displayed on an oscilloscope where the signals' first peak arrival times were measured. The signal peak frequency was 1 MHz. The wave speeds of the compressional and shear modes were calculated by dividing the time of arrival of a particular propagation mode into the length of the sample. Corrections, due to small inherent signal delay times, were applied to the signal arrival times prior to the velocity calculations. The density of each sample was calculated from the ratio of weight to volume, where the bulk volume was calculated from independent caliper measurements of sample length and diameter.

The dynamic Poisson's Ratio and Young's Modulus were calculated from the ultrasonic wave velocities (both p-wave and s-wave) and bulk density using Equations (5) and (6). These relations, although exact only for core materials that possess linear elastic, homogeneous, and isotropic behavior, are employed universally throughout the industry, and usually provide reasonable estimates of the dynamic elastic moduli. The dynamic Poisson's Ratio (ν) was calculated from the expression:

$$\nu = (0.5(V_p/V_s)^2 - 1)/((V_p/V_s)^2 - 1) \quad (5)$$

V_p and V_s are the compressional and shear wave velocities, respectively. The dynamic Young's Modulus (E) was calculated from the expression:

$$E = 2\rho_b(V_s)^2 (1 + \nu) \quad (6)$$

ρ_b is the bulk density of the sample. The test results of the stress dependent ultrasonic wave velocities are located in Appendix I.

Static Elastic Moduli

Triaxial or confined tests were performed using a pressure vessel that has a lower one-inch diameter interior steel pedestal for mounting a sleeved core sample. An upper steel movable piston was inserted into the top portion of the rubber sleeve. The piston contacts the core and extends out the top of the vessel. The pressure vessel was placed in the mechanical press, where the axial load to the core was applied through the movable piston. A circumferential displacement gauge was wrapped around the rubber sleeve and used to measure the change in circumference of the core. Confining stress was supplied by hydraulic oil that fills the vessel and pressurized using a programmable pump. Two LVDT's mounted external to the pressure vessel were used to measure the change in length of the core via displacement of the movable piston.

The stress path followed was identical to that used in measuring the dynamic elastic moduli. The static and dynamic elastic property measurements were made concurrent to each other. Confining stress was set to 2000 psi. The hydrostatic stress was ramped at a rate of about 100 psi/minute. The axial deviatoric stress was ramped to nearly 6000 psi at a rate of 640 psi/minute. The axial deviatoric stress path was cycled twice to remove stress hysteresis effects from the measurements.

The axial stress was calculated from the ratio of axial force to sample cross-sectional area. The uncorrected axial strain was calculated from the ratio of the average displacements of the two axial LVDT's to the initial sample length. Since the two LVDT's were mounted external to the pressure vessel, the total axial deformation included some deformation from the steel platens and spherical seat of the test frame. The axial strain was corrected by subtracting out the effect of the platens using the relation:

$$\varepsilon_c = \varepsilon_m - \Delta\sigma\ A/(Lb) \qquad (7)$$

ε_m is measured strain, $\Delta\sigma$ is the change in axial stress, A is the sample cross-sectional area, L is the initial sample length, and "b" is the compliance of the platens and test frame, defined as $\Delta F/\Delta x$, where ΔF is the force required to cause a displacement, Δx, in the platens and test frame. The "b" compliance factor was actually determined by measuring the Young's modulus of an aluminum standard whose elastic properties are known. "b" was then inferred from the expression:

$$1/E_{al} = 1/\ E_{al}' - A_{al}/(L_{al}b) \qquad (8)$$

The "b" compliance factor was determined over the stress interval at which the Young's modulus was calculated.

Young's modulus (E) was calculated from the slope of the increasing axial stress versus axial strain curve of the 2nd stress cycle.

$$E = \Delta\sigma/\Delta\varepsilon_c \quad (9)$$

The radial strain is expressed as:

$$\varepsilon_r = -\gamma\Delta C/(\pi D) \quad (10)$$

ΔC is the change in circumference of the sample, which is directly measured by the circumferential LVDT. Note that an increase in circumference (i.e. positive ΔC) produces a negative radial strain. D is the sample's initial diameter. The factor, γ, is used to compensate for a systematic error (geometric) introduced by the circumferential LVDT. The Poisson's Ratio was calculated from the secant slope of the radial versus axial strain curve of the 2nd stress cycle.

$$\nu = -\Delta\varepsilon_r/\Delta\varepsilon_c \quad (11)$$

The volumetric strain ($\varepsilon_c + 2\varepsilon_r$) was monitored during the tests. The cores initially go through a compaction phase where the volume of the sample decreases with increasing axial load. As the axial load continues to increase, a point is usually reached where the volume strain begins to increase with additional loading. This turning point in the volume versus axial strain curve represents the start of dilation and the beginning of non-elastic behavior (and sometimes sample failure). This turning point was also used to define the portion of the curve used to calculate the Poisson's Ratio. All calculations of Poisson's Ratio were determined along the compaction portion of the radial versus axial strain curve. No cores were observed to go into dilation under the applied loads used in these tests. The stress-strain curves of each sample are located in Appendix II.

Brinell Hardness Measurements

Brinell Hardness (formation hardness) was measured using an ELE steel ball penetrometer. The device consists of a single steel ball attached to a stationary plate and rod. The core sample to be tested sits on pedestal beneath the steel ball. A calibrated load-ring is connected in series to the steel ball and plate and measures the load at the steel ball/core interface as the sample is raised up against the steel ball. The ball diameter used in these tests was 0.061 inches. A micrometer was used to measure the displacement of the steel ball as is penetrates the core sample. In addition, a digital photograph of the indentations (and a millimeter scale) was recorded. The cross-sectional area (A) of each indentation was measured using measurement tools provided by the freeware program ImageJ.

Brinell Hardness was determined by measuring the displacement versus load of a steel ball as it penetrated the smooth surface of a core sample. Brinell Hardness (BH) is defined as the ratio of load (force) to the contact area (A_i) of the indentation from the steel ball.

$$BH = F/A_i \quad (12)$$

The contact area, A_i , was calculated from the expression:

$$A_i = \pi D_b H \quad (13)$$

The penetration distance, H, was calculated from the cross-sectional area (A) of the indentation using the expression:

$$H = (D_b - \text{sqrt}\{D_p^2 - d^2\})/2 \quad (14)$$

D_b is the ball diameter, and d is the diameter of the measured cross-sectional area (A) of the indentation.

$$d = 2\text{sqrt}\{A/\pi\} \quad (15)$$

The BH values at three different locations on core surface were measured and averaged to obtain the average BH value and standard deviation of the core as reported in Table 3.

REFERENCES

[1] TTC Report No. 06-10-0906, "Analysis of Wholecore Segments", BJ Davis & L. Vestal, December 21, 2006.

[2] TTC Report No. 06-10-0906SCA "Acid Flow Testing", C. De Vine, February 12, 2007.

Technology Center Report No.	**06-10-906RM**	Reported by: R.L. Maharidge
Requested by:	Mr. Roger Myers	
Location:	Pittsburgh, PA	
Contributors:	N. Knudson – Rock Mechanics, BH Measurements, Photography J. Boles - Acid Treatments M. Vorderbruggen – Acid Treatments R. Maharidge – Data Reduction and Reporting	
Distribution:	Roger Myers, Dan Kendrick, Brian Davis, TTC file.	

APPENDIX I

STRESS DEPENDENT ULTRASONIC WAVE VELOCITY DATA

Table I-A displays the stress dependent inverse compressional and shear wave velocity data for each of the samples. The dynamic Young's Modulus and Poisson's Ratio are also displayed. The inverse wave velocities and dynamic elastic moduli were cross-plotted against net mean stress for each sample. The cross-plots were used to perform least square fits to the data so that the elastic moduli could be extrapolated to reservoir net mean stress. The extrapolated values are shown in "bold" type in the table. The extrapolated data are also reported in Table 4 in the main body of this report.

Table I-A
Dynamic Elastic Properties of Core from the Big Lime Formation

Sample	Net Mean Stress (psi)	Density (g/cc)	Poisson's Ratio	Young's Modulus ($x10^6$ psi)	Inverse P-wave Velocity (μsec/ft)	Inverse S-wave Velocity (μsec/ft)
C	2004	2.609	0.302	8.73	54.5	102.4
	3255	2.609	0.309	8.78	53.8	102.4
	2004	2.609	0.307	8.77	54.0	102.4
	3255	2.609	0.312	8.80	53.5	102.4
	2004	2.609	0.309	8.78	53.8	102.4
	611		**0.305**	**8.76**	**54.2**	**102.4**
F	2004	2.740	0.288	10.02	53.1	97.4
	3255	2.740	0.301	10.25	51.7	96.8
	2004	2.740	0.290	10.16	52.6	96.8
	3255	2.740	0.296	10.20	52.1	96.8
	2004	2.740	0.290	10.16	52.6	96.8
L	**611**		**0.281**	**10.1**	**53.5**	**96.8**
	2004	2.529	0.238	7.53	62.0	105.8
	3255	2.529	0.240	7.63	61.5	105.2
	2004	2.529	0.242	7.55	61.8	105.8
	3255	2.529	0.246	7.67	61.1	105.2
	2004	2.529	0.242	7.55	61.8	105.8
	612		**0.240**	**7.44**	**62.3**	**106.5**
N	2004	2.443	0.246	6.67	64.3	110.9
	3255	2.443	0.250	6.84	63.3	109.6
	2004	2.443	0.248	6.76	63.8	110.3
	3255	2.443	0.250	6.84	63.3	109.6
	2004	2.443	0.248	6.76	63.8	110.3
	612		**0.246**	**6.66**	**64.4**	**110.9**

Table I-A
Dynamic Elastic Properties of Core from the Big Lime Formation

Sample	Net Mean Stress (psi)	Density (g/cc)	Poisson's Ratio	Young's Modulus ($x10^6$ psi)	Inverse P-wave Velocity (μsec/ft)	Inverse S-wave Velocity (μsec/ft)
V	2004	2.658	0.270	9.33	55.4	98.7
	3255	2.658	0.283	9.67	53.7	97.5
	2004	2.658	0.278	9.51	54.4	98.1
	3255	2.658	0.285	9.69	53.4	97.5
	2004	2.658	0.278	9.51	54.4	98.1
	613		**0.271**	**9.33**	**55.4**	**98.8**
Y	2002	2.679	0.273	10.23	52.9	94.8
	3251	2.679	0.278	10.40	52.2	94.2
	2002	2.679	0.272	10.35	52.7	94.2
	3251	2.679	0.275	10.37	52.5	94.2
	2002	2.679	0.269	10.32	52.9	94.2
	613		**0.263**	**10.28**	**53.4**	**94.2**
CC	2002	2.706	0.284	10.32	52.3	95.2
	3251	2.706	0.292	10.52	51.3	94.6
	2002	2.706	0.286	10.47	51.8	94.6
	3251	2.706	0.292	10.52	51.3	94.6
	2002	2.706	0.289	10.50	51.6	94.6
	613		**0.282**	**10.44**	**52.1**	**94.6**
GG	2002	2.562	0.260	7.96	59.5	104.5
	3255	2.740	0.279	9.12	56.4	101.8
	2004	2.740	0.270	8.83	57.8	103.0
	3255	2.740	0.279	9.12	56.4	101.8
	2004	2.740	0.270	8.83	57.8	103.0
	614		**0.259**	**8.53**	**59.5**	**104.4**
KK	2002	2.546	0.264	7.21	62.1	109.7
	3251	2.546	0.289	7.97	57.4	105.3
	2002	2.546	0.276	7.62	59.6	107.2
	3251	2.546	0.287	7.95	57.6	105.3
	2002	2.546	0.279	7.63	59.4	107.2
	614		**0.266**	**7.27**	**61.7**	**109.3**

Table I-A
Dynamic Elastic Properties of Core from the Big Lime Formation

Sample	Net Mean Stress (psi)	Density (g/cc)	Poisson's Ratio	Young's Modulus ($x10^6$ psi)	Inverse P-wave Velocity (μsec/ft)	Inverse S-wave Velocity (μsec/ft)
UU	2002	2.453	0.248	5.84	68.8	118.8
	3251	2.453	0.278	6.72	62.2	112.1
	2002	2.453	0.266	6.38	64.6	114.5
	3251	2.453	0.274	6.78	62.2	111.4
	2002	2.453	0.271	6.41	64.1	114.5
	615		**0.261**	**6.02**	**66.9**	**117.6**
YY	2004	2.656	0.296	9.04	54.5	101.3
	3255	2.656	0.297	9.28	53.8	100.0
	2004	2.656	0.295	9.15	54.3	100.6
	3255	2.656	0.297	9.28	53.8	100.0
	2004	2.656	0.298	9.17	54.0	100.6
	617		**0.296**	**9.03**	**54.6**	**101.3**
WW	2002	2.710	0.307	8.40	56.3	106.5
	3251	2.710	0.313	9.28	53.1	101.6
	2002	2.710	0.312	9.06	53.8	102.8
	3251	2.710	0.315	9.30	52.8	101.6
	2002	2.710	0.312	9.06	53.8	102.8
	617		**0.309**	**8.80**	**54.8**	**104.2**

APPENDIX II

STRESS-STRAIN CURVES FROM TRIAXIAL STATE OF STRESS TESTS

The following pages contain the stress-strain curves from which Young's modulus and Poisson's Ratio were calculated. Each page contains two figures: the top figure presents the axial stress versus axial strain curve for determining Young's modulus; the lower figure presents the radial versus axial strain for determining Poisson's Ratio. Positive strain indicates contraction, while negative strain indicates expansion. Each figure shows both axial loading cycles. The elastic moduli were determined along the increasing axial stress path of the 2nd stress cycle. The data points used in determining the moduli are shown in red.

Figure II-1
Young's Modulus of Sample C

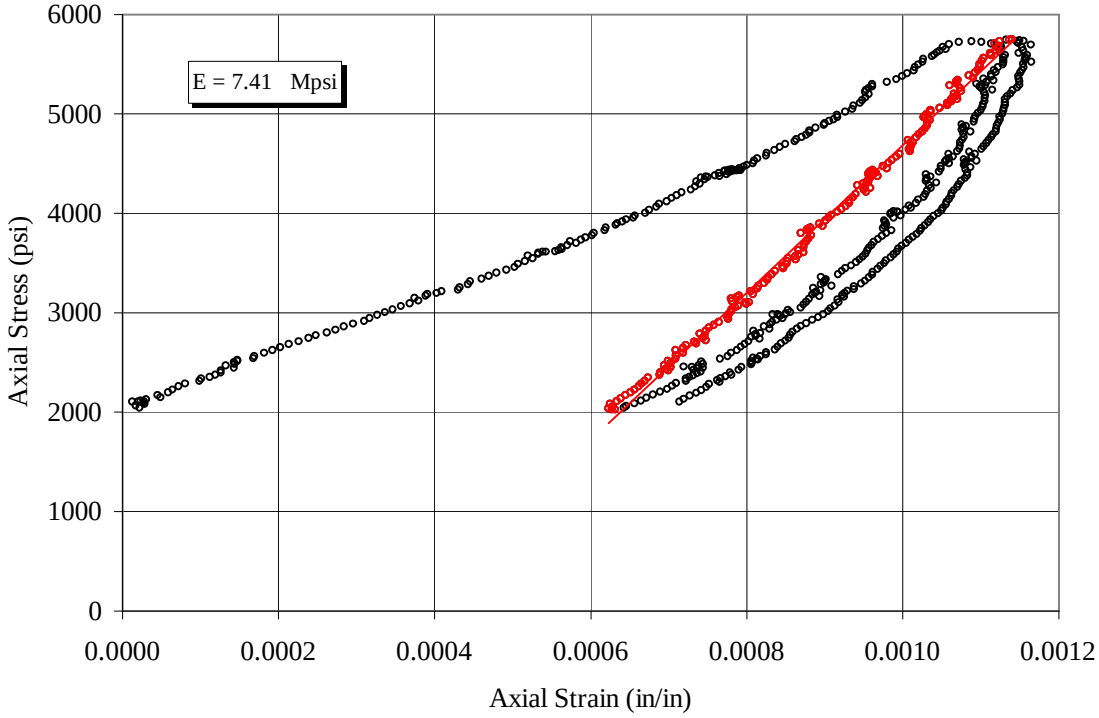

Figure II-2
Poisson's Ratio of Sample C

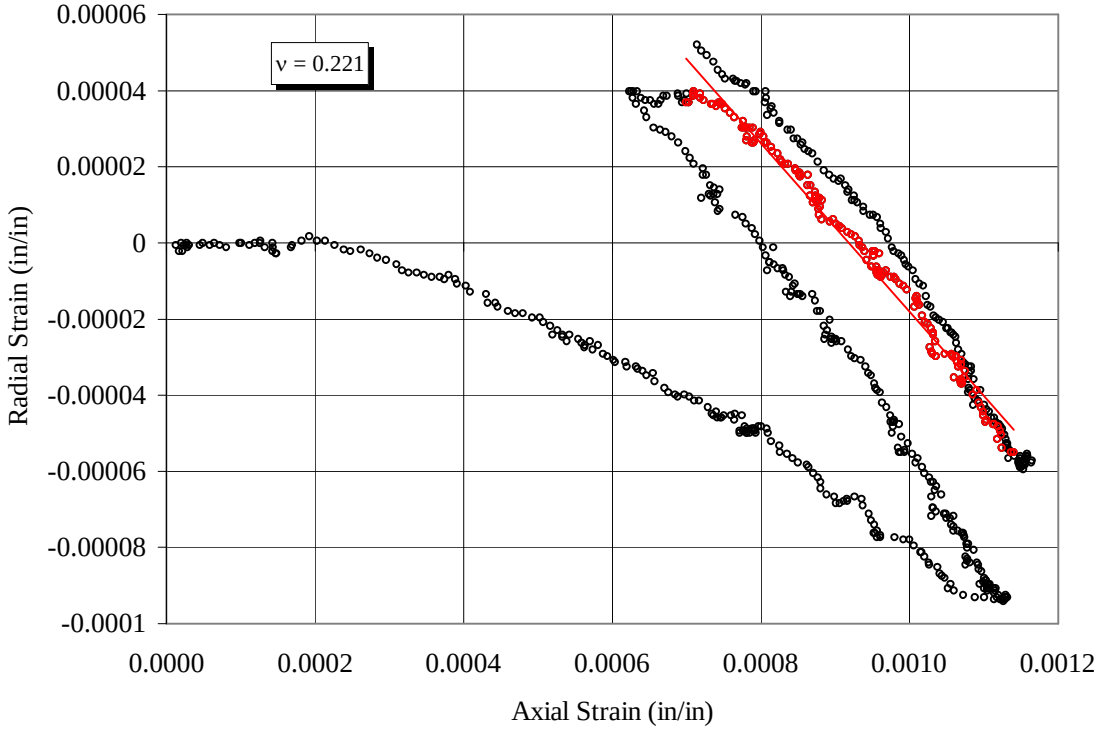

Figure II-3
Young's Modulus of Sample F

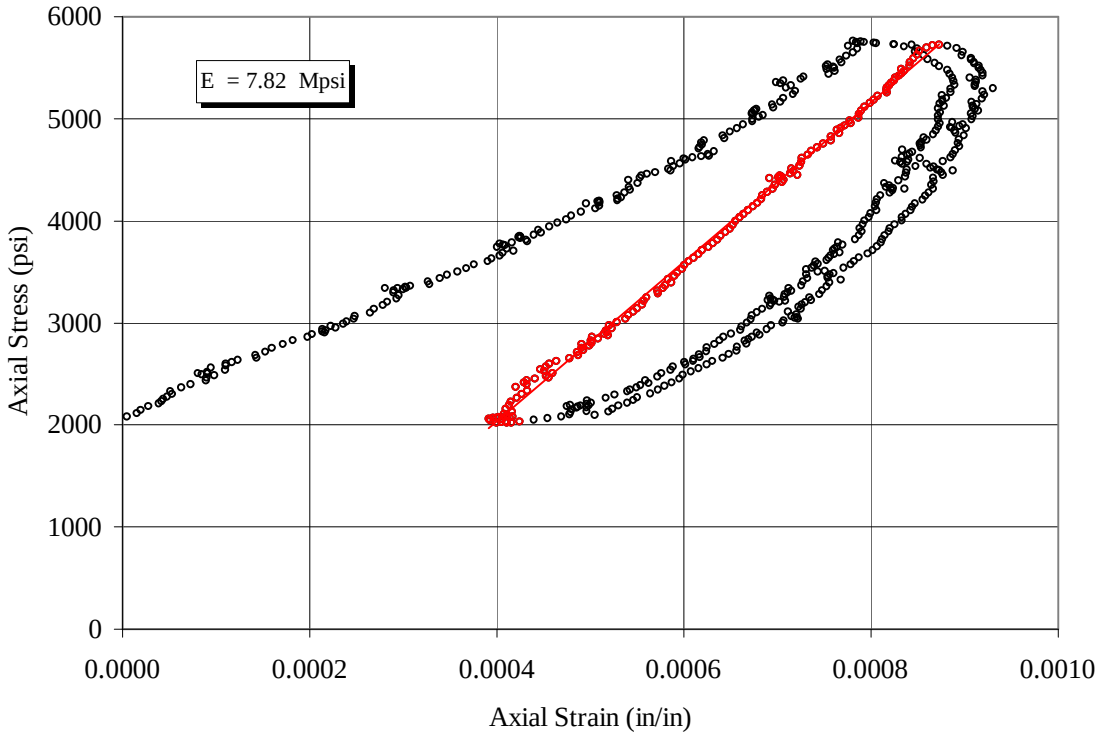

Figure II-4
Poisson's Ratio of Sample F

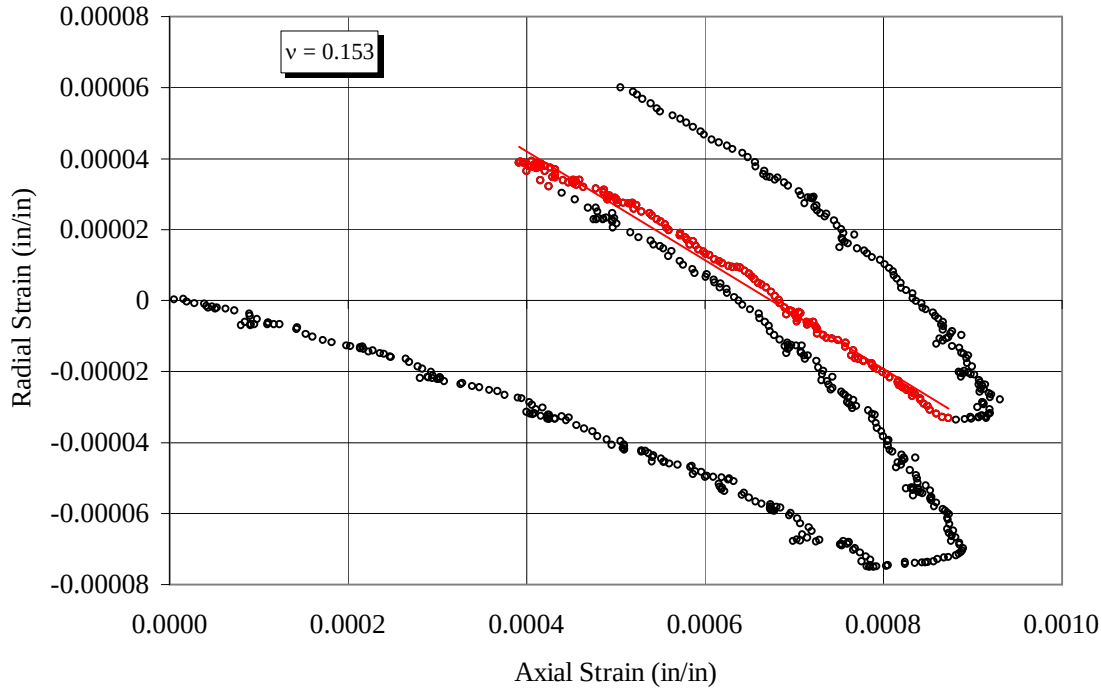

Figure II-5
Young's Modulus of Sample L

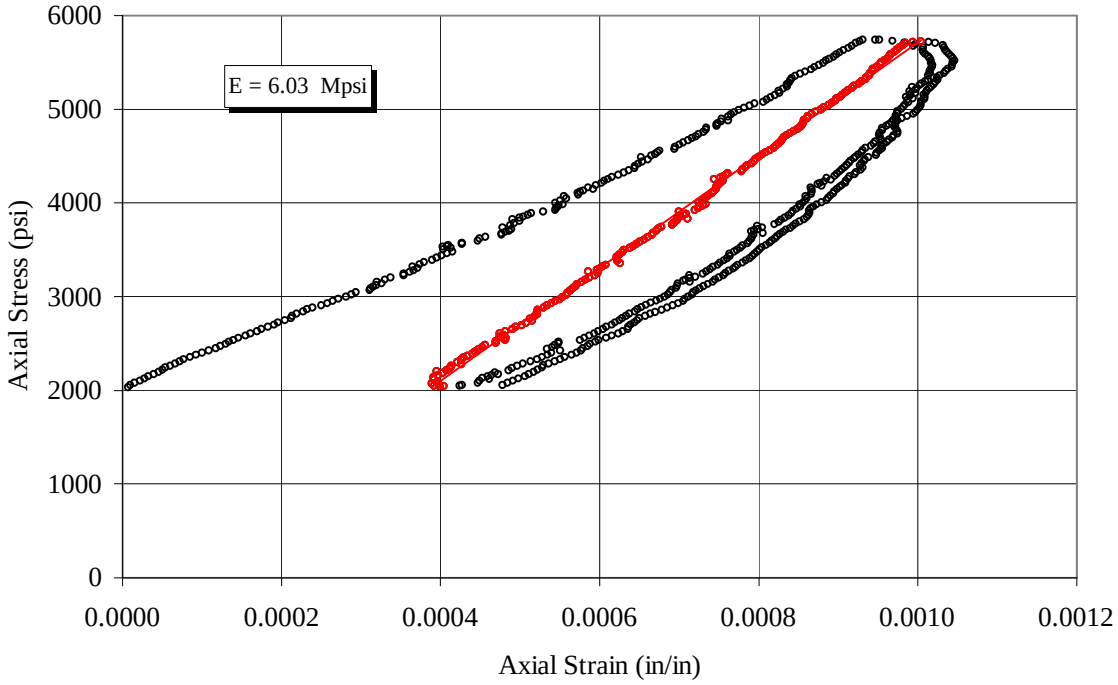

Figure II-6
Poisson's Ratio of Sample L

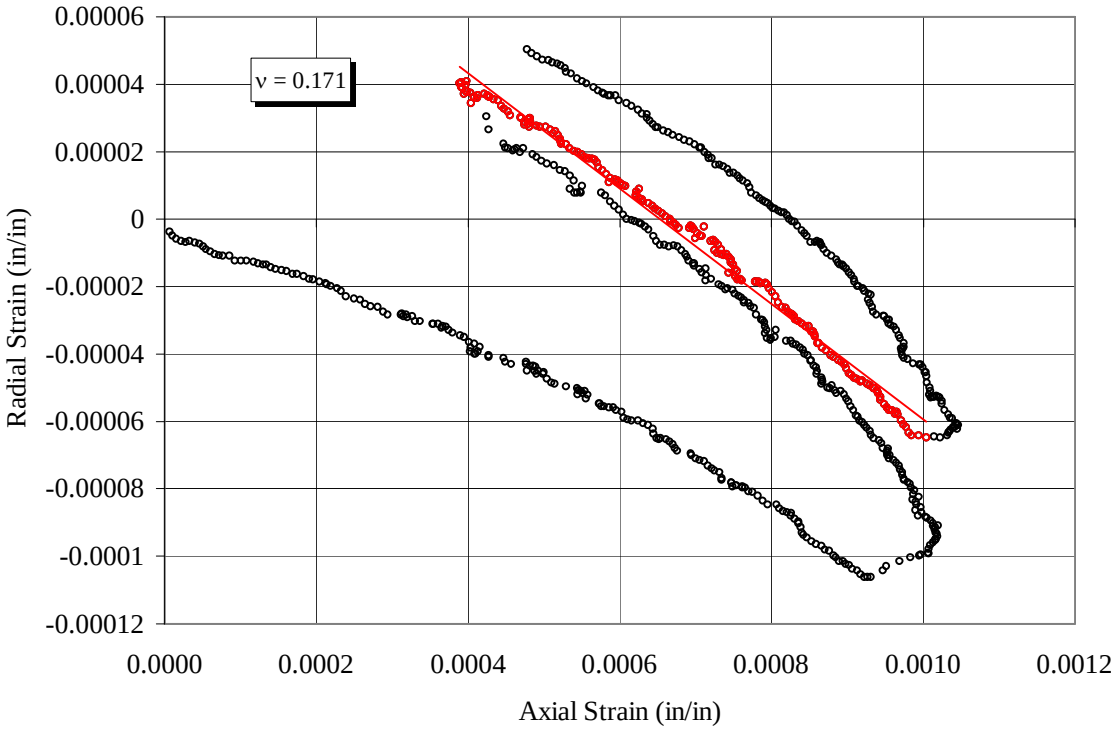

Figure II-7
Young's Modulus of Sample N

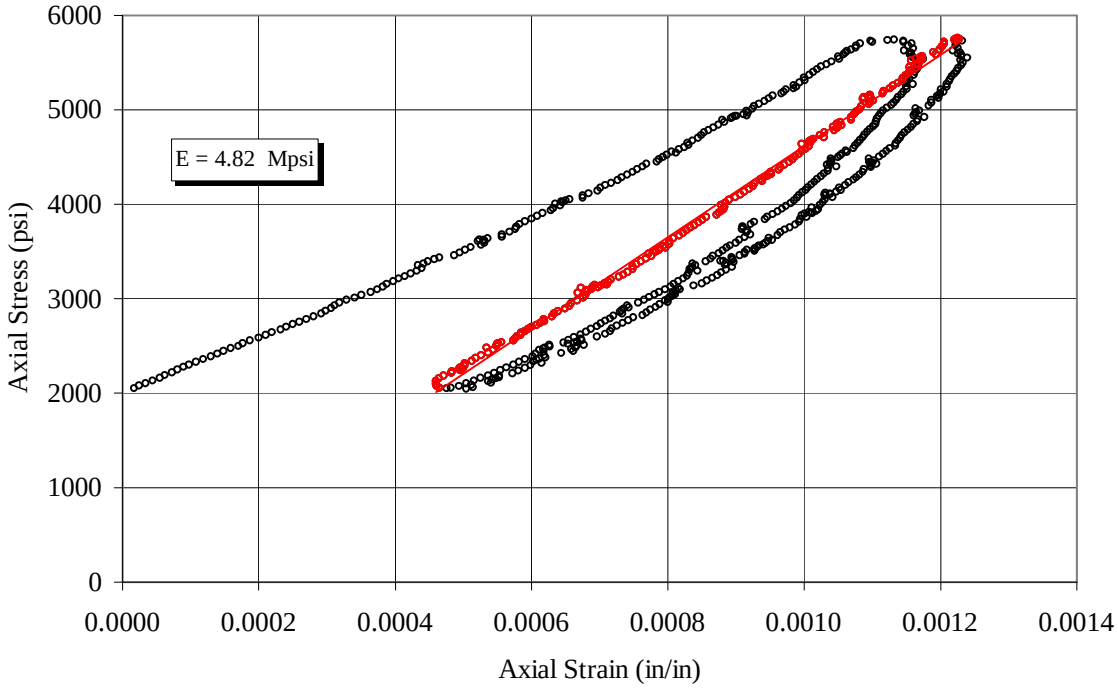

Figure II-8
Poisson's Ratio of Sample N

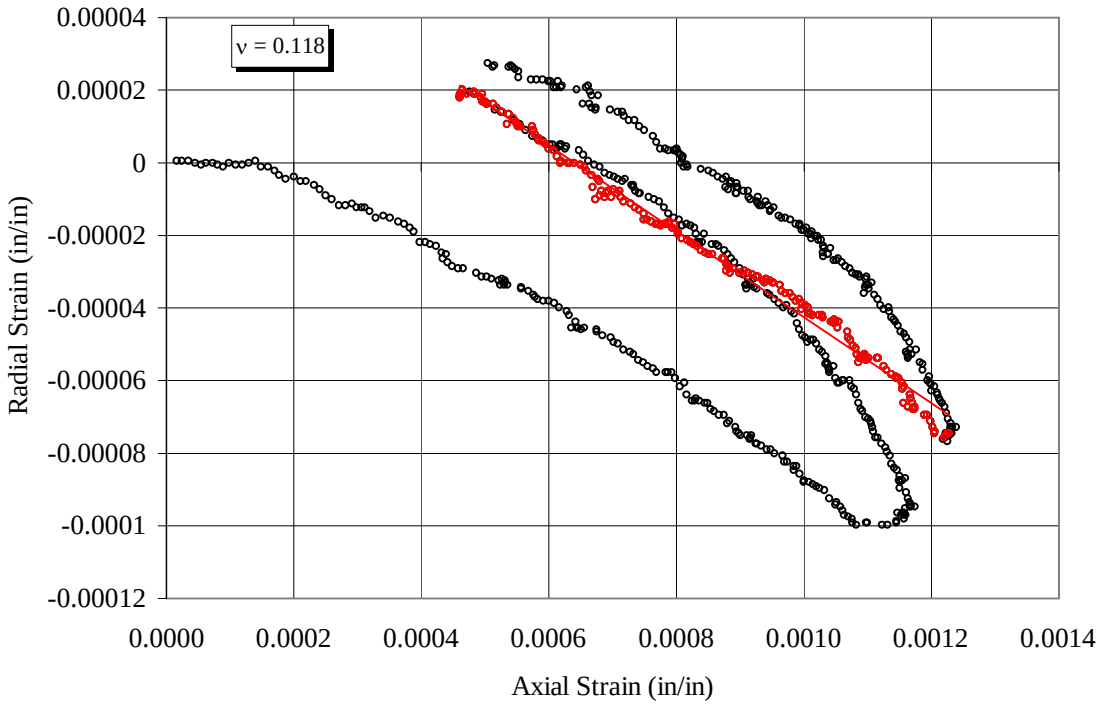

Figure II-9
Young's Modulus of Sample V

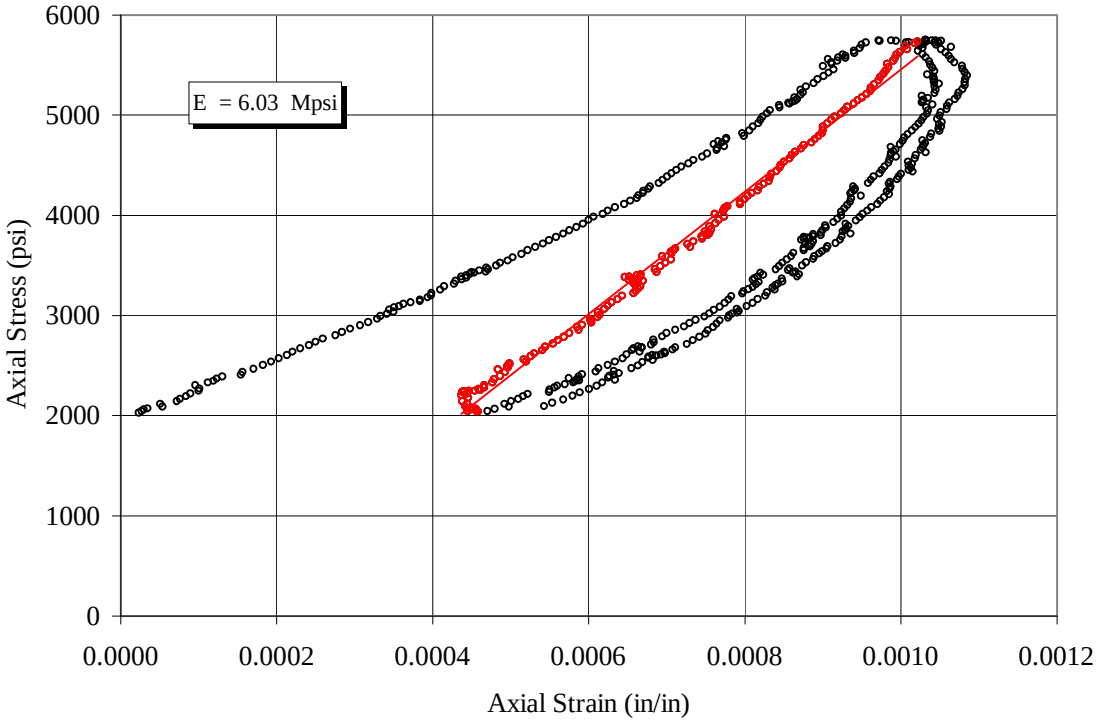

Figure II-10
Poisson's Ratio of Sample V

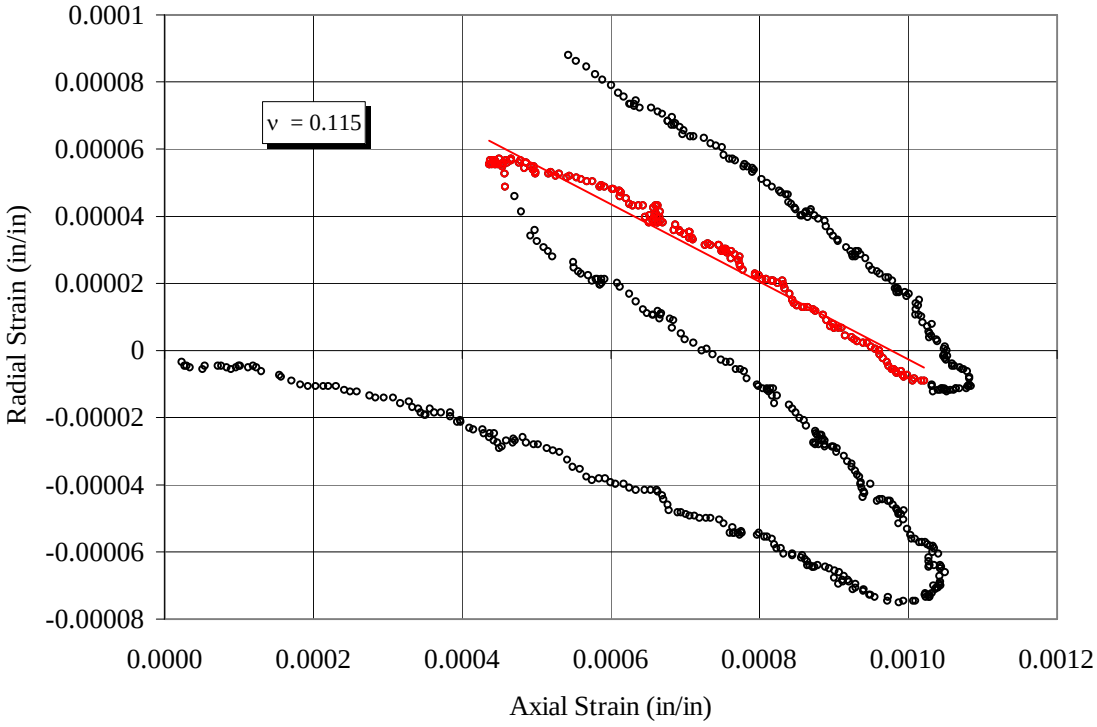

Figure II-11
Young's Modulus of Sample Y

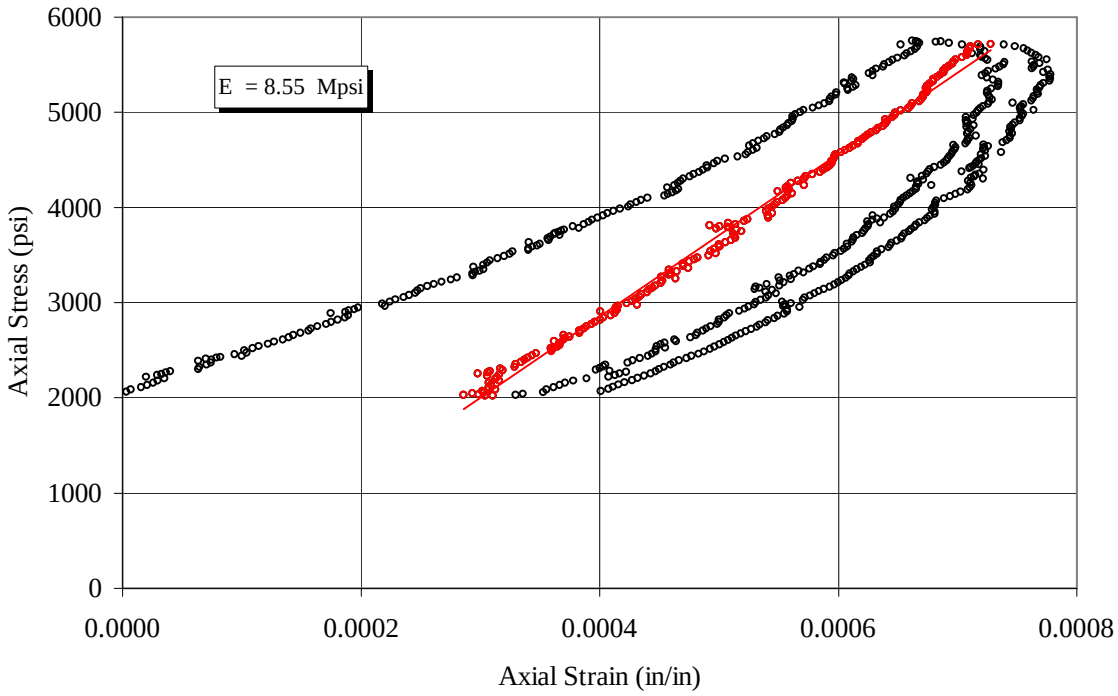

Figure II-12
Poisson's Ratio of Sample Y

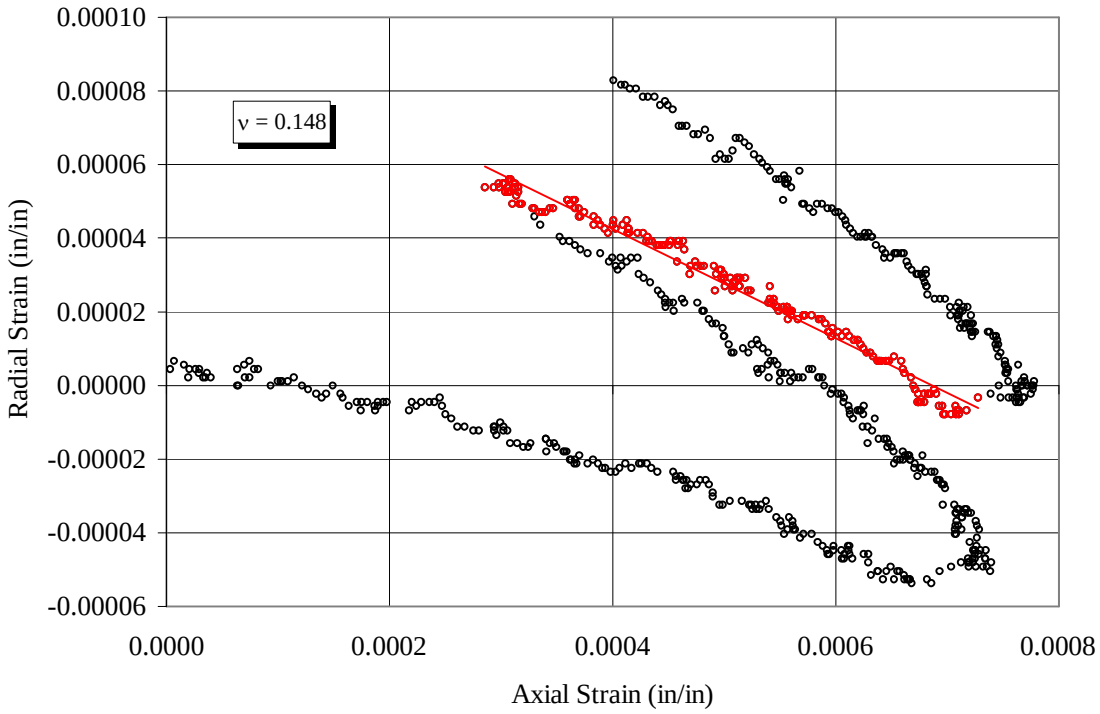

Figure II-13
Young's Modulus of Sample CC

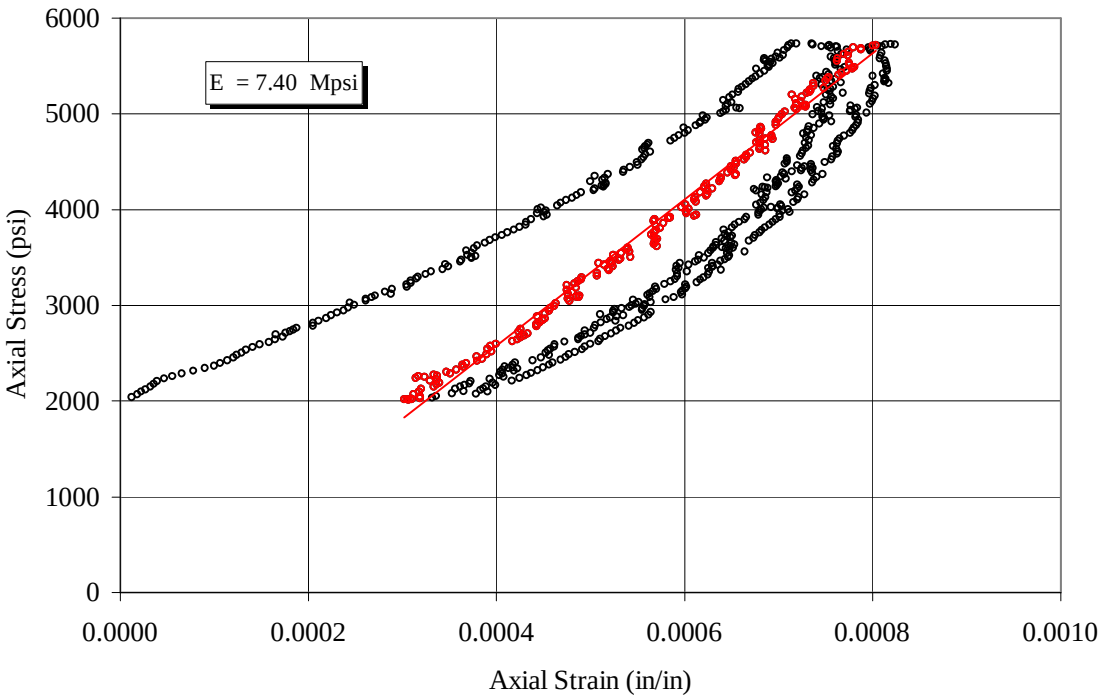

Figure II-14
Poisson's Ratio of Sample CC

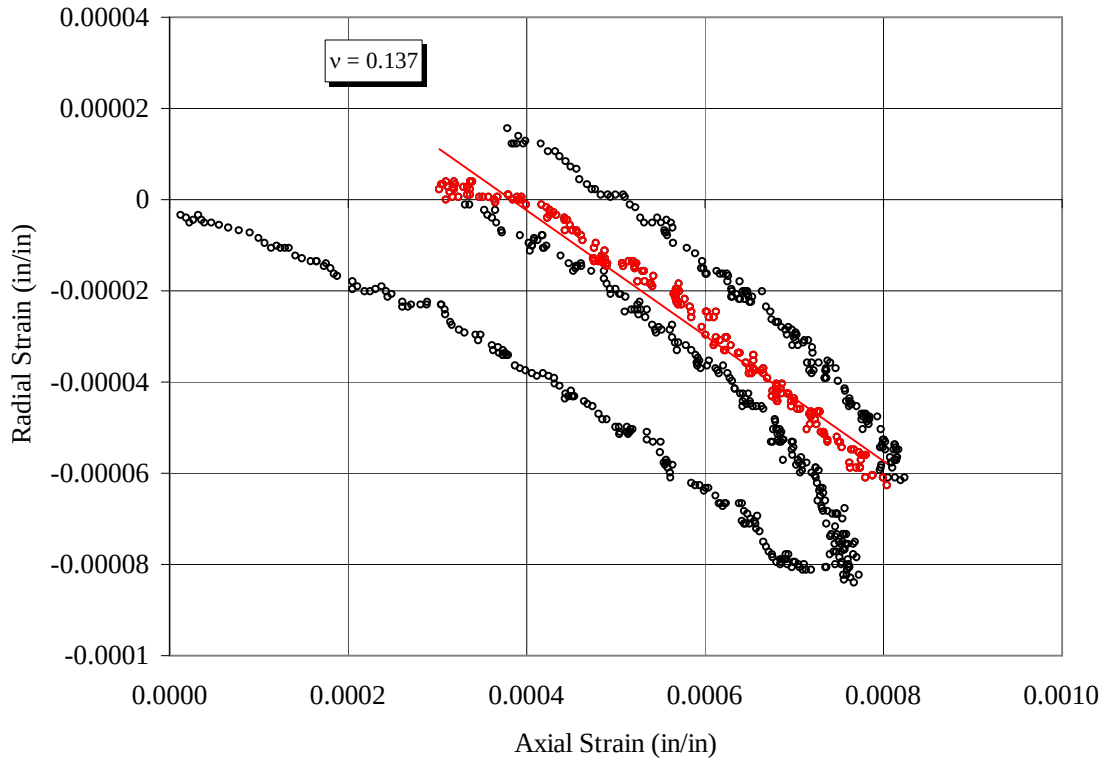

Figure II-15
Young's Modulus of Sample GG

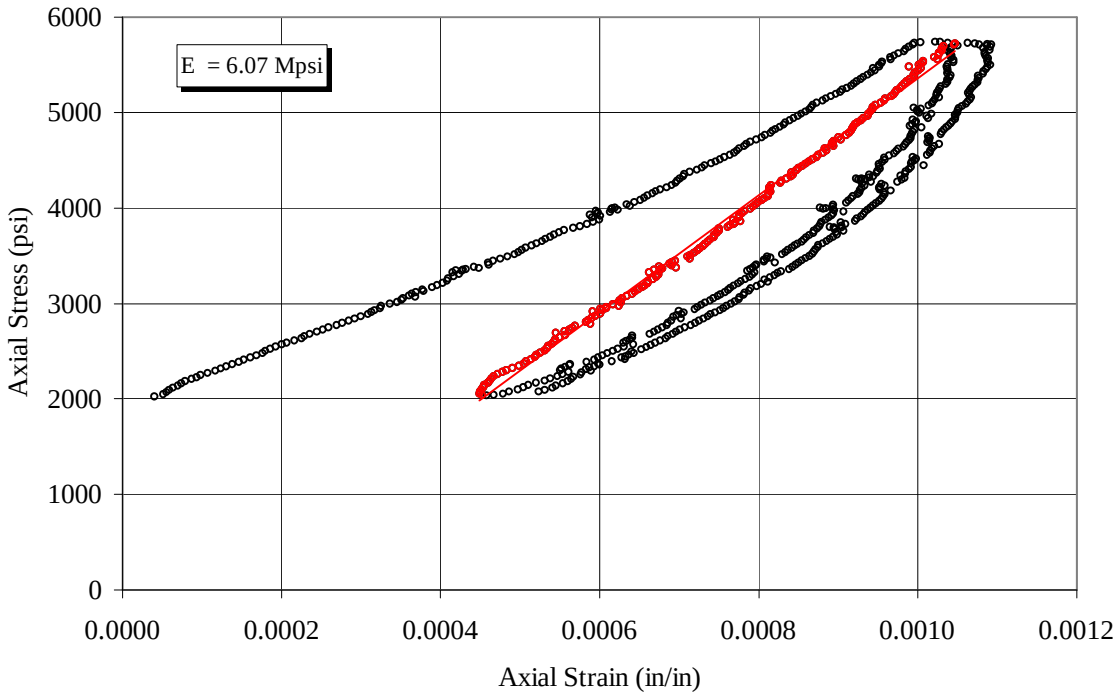

Figure II-16
Poisson's Ratio of Sample GG

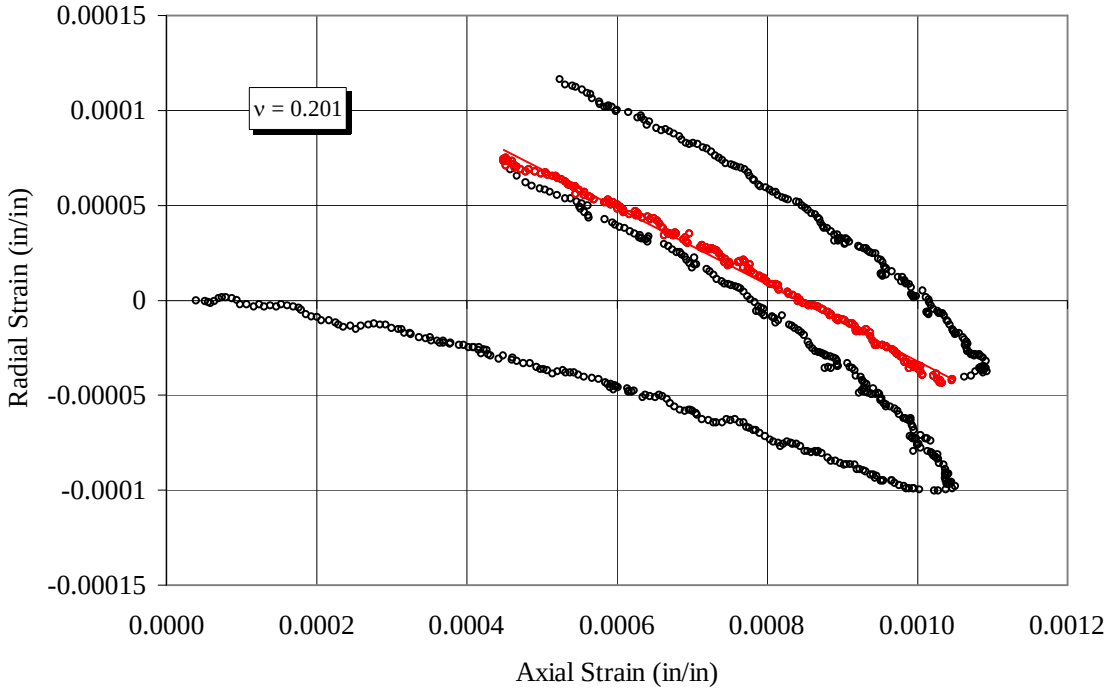

Figure II-17
Young's Modulus of Sample KK

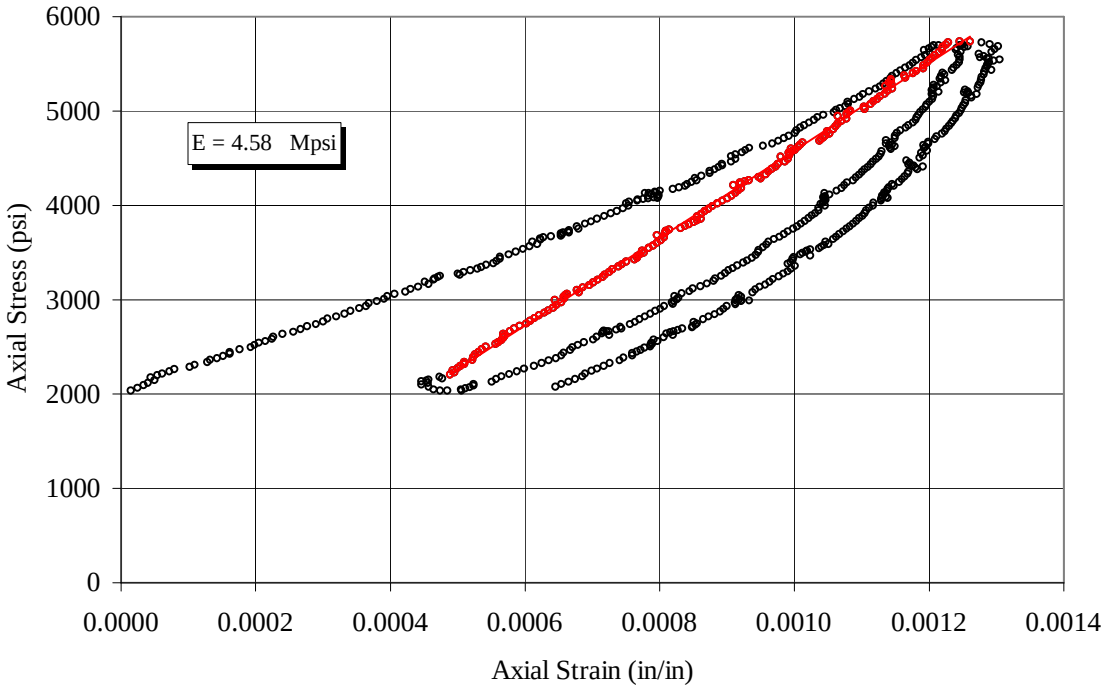

Figure II-18
Poisson's Ratio of Sample KK

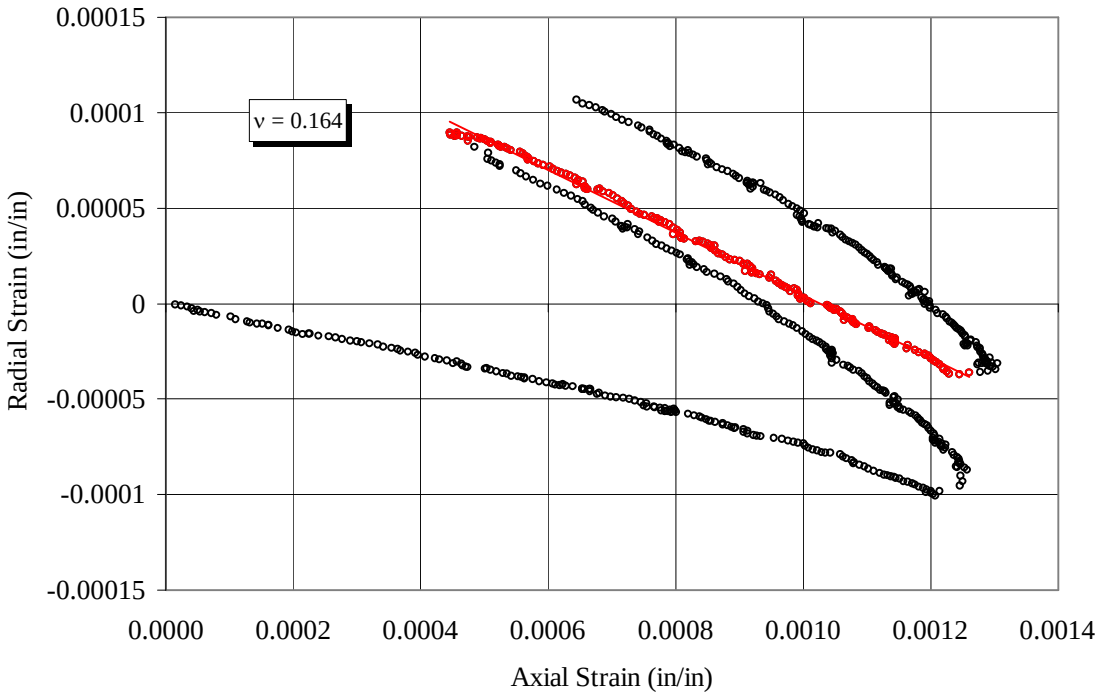

Figure II-19
Young's Modulus of Sample UU

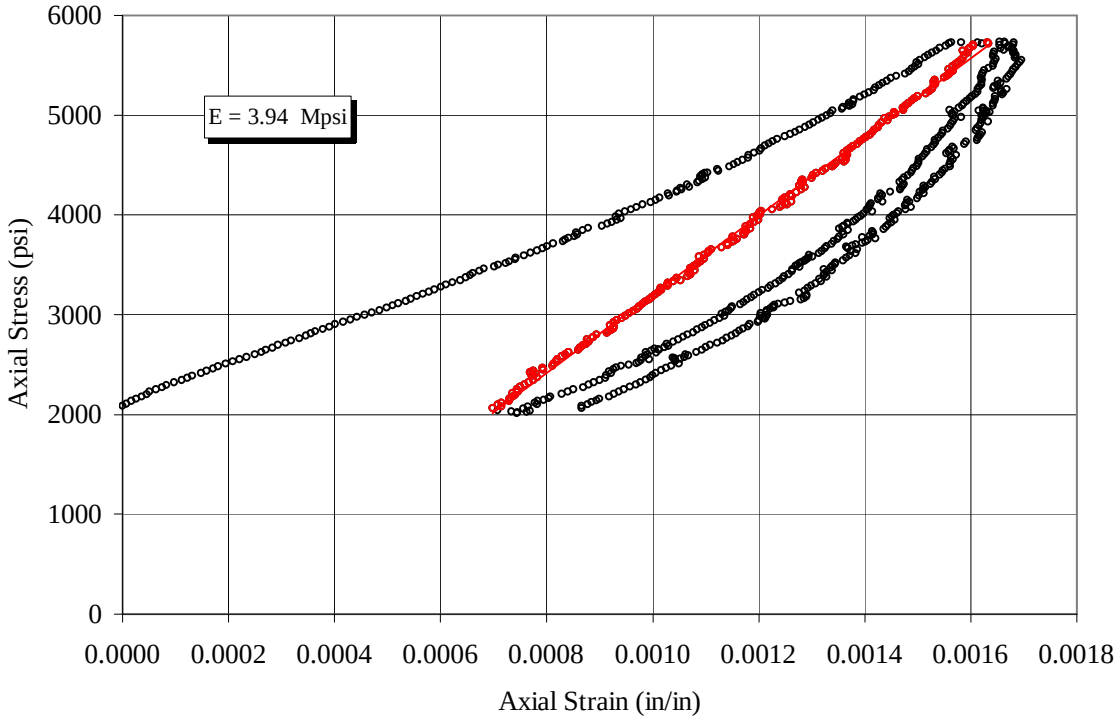

Figure II-20
Poisson's Ratio of Sample UU

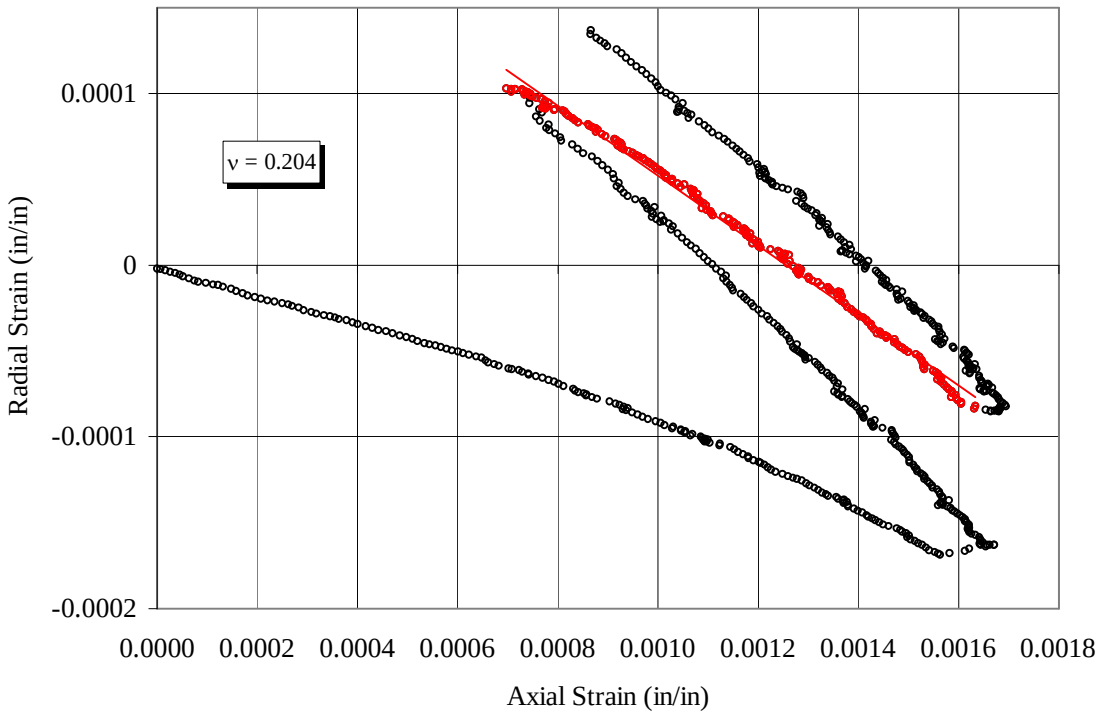

Figure II-21
Young's Modulus of Sample WW

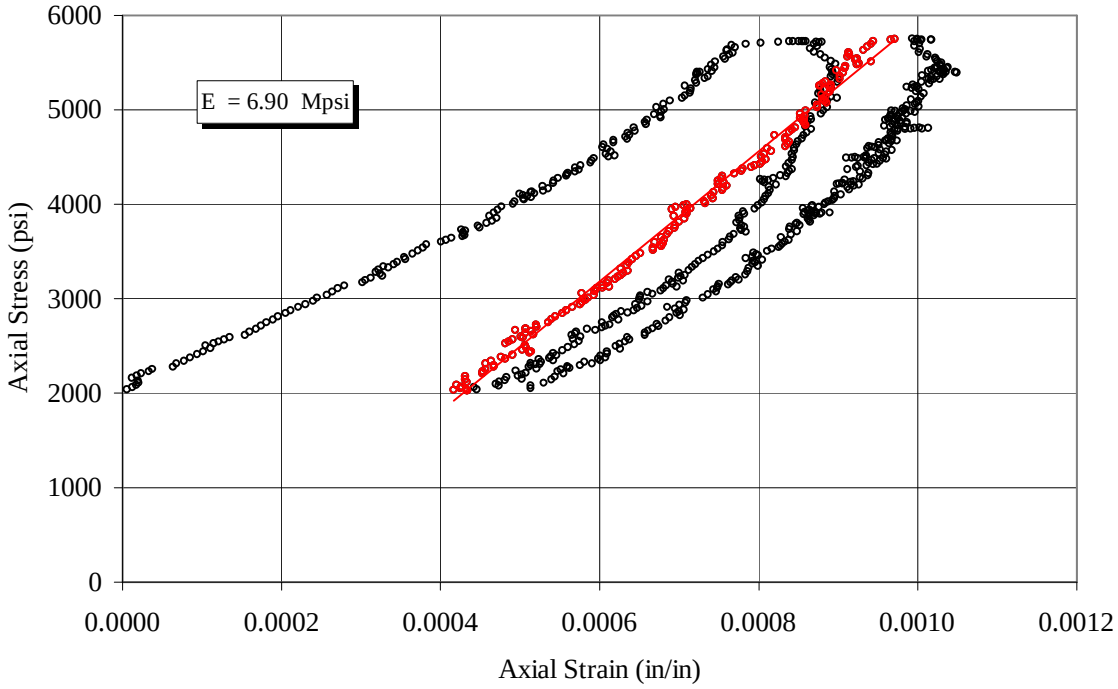

Figure II-22
Poisson's Ratio of Sample WW

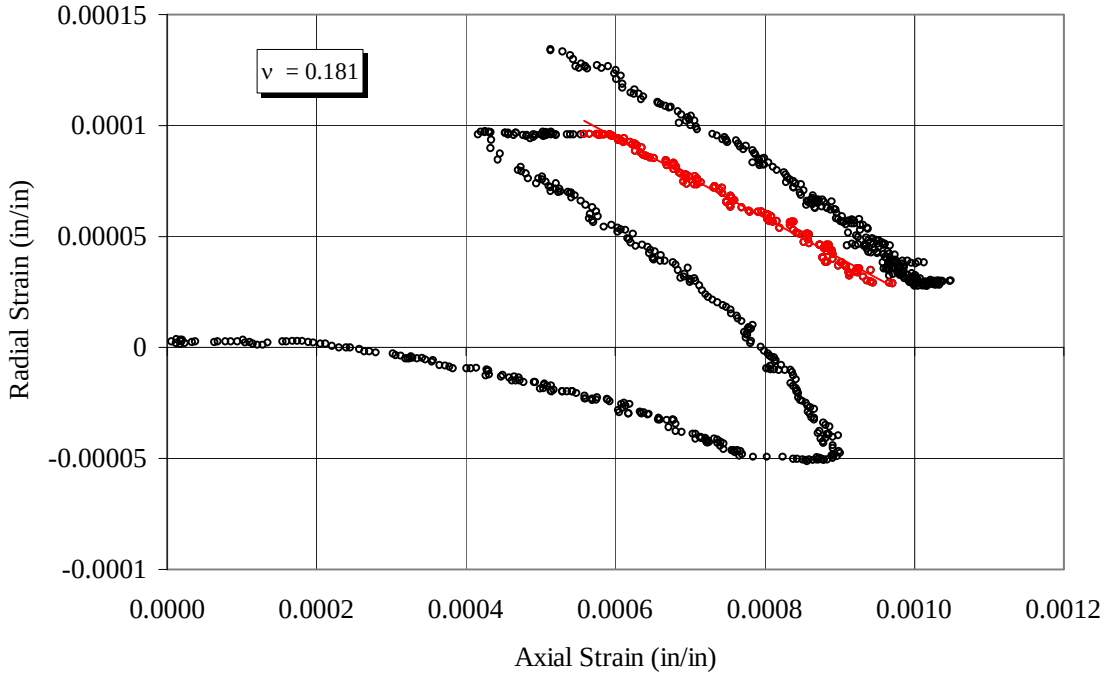

Figure II-23
Young's Modulus of Sample YY

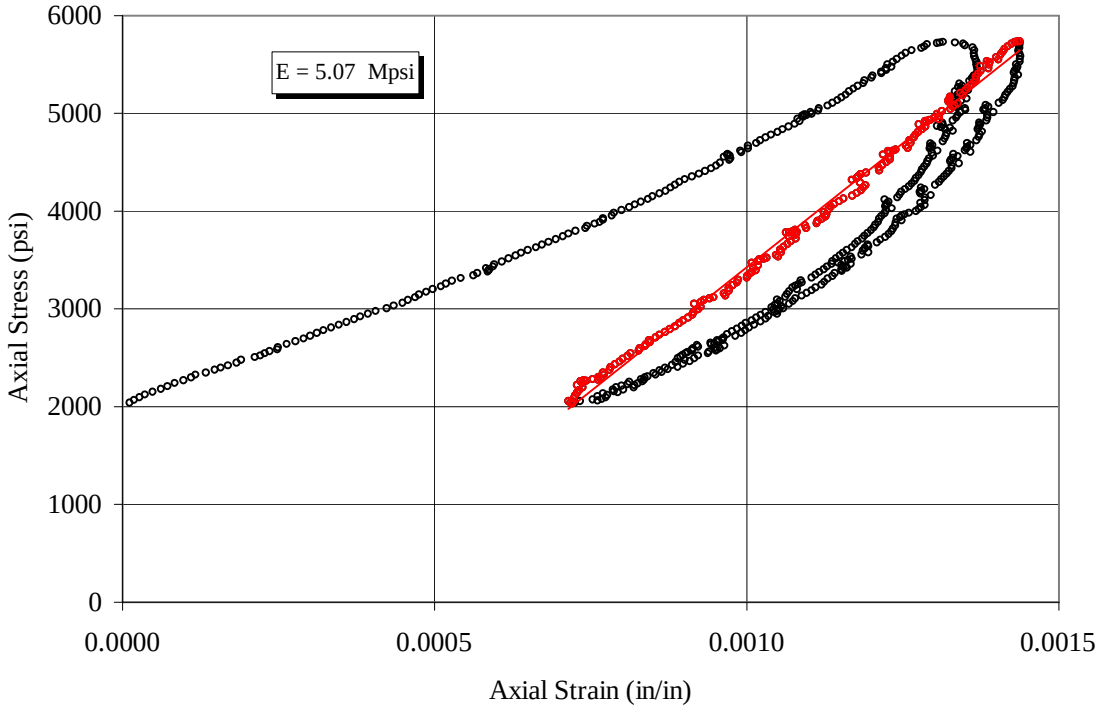

Figure II-24
Poisson's Ratio of Sample YY

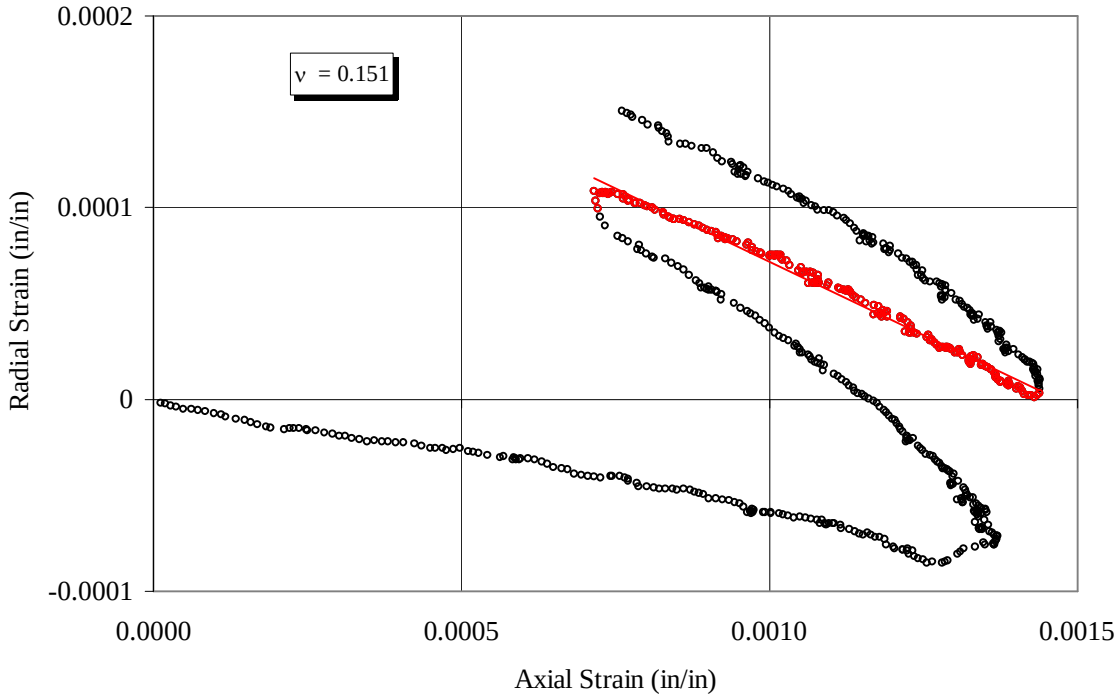

APPENDIX III

PHOTOGRAPHS OF SURFACES OF PRE/POST ACID EXPOSED CORE PLUGS

Pre-Exposed Surface (Sample KK)

15% HCl Exposed Surface (Sample KK)

3 minute exposure time

6 minute exposure time

Note quartz grains and coarse texture

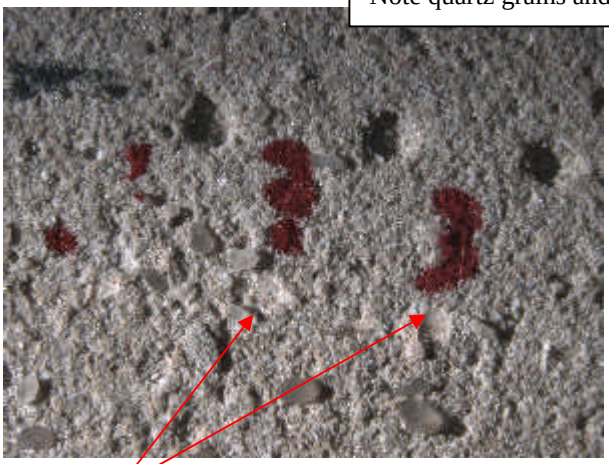

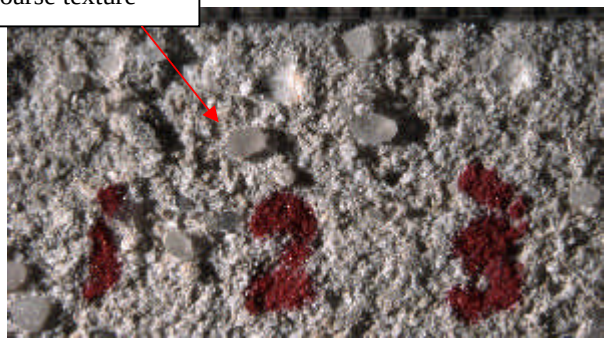

indentations

9 min exposure

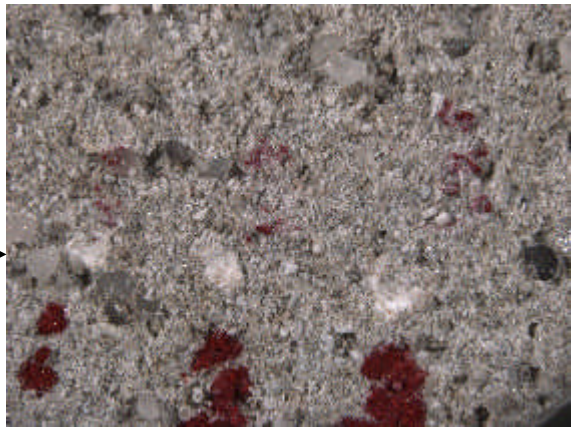

Pre-Exposed Surface

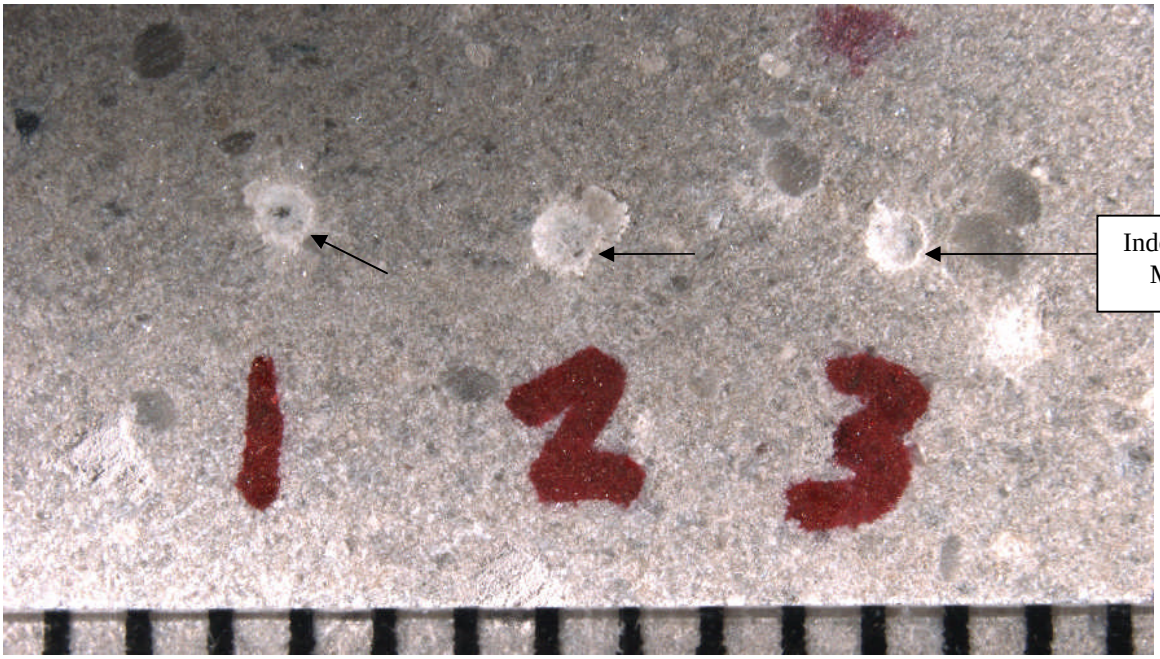

Foam-Acid Exposed Surface (24 minutes)

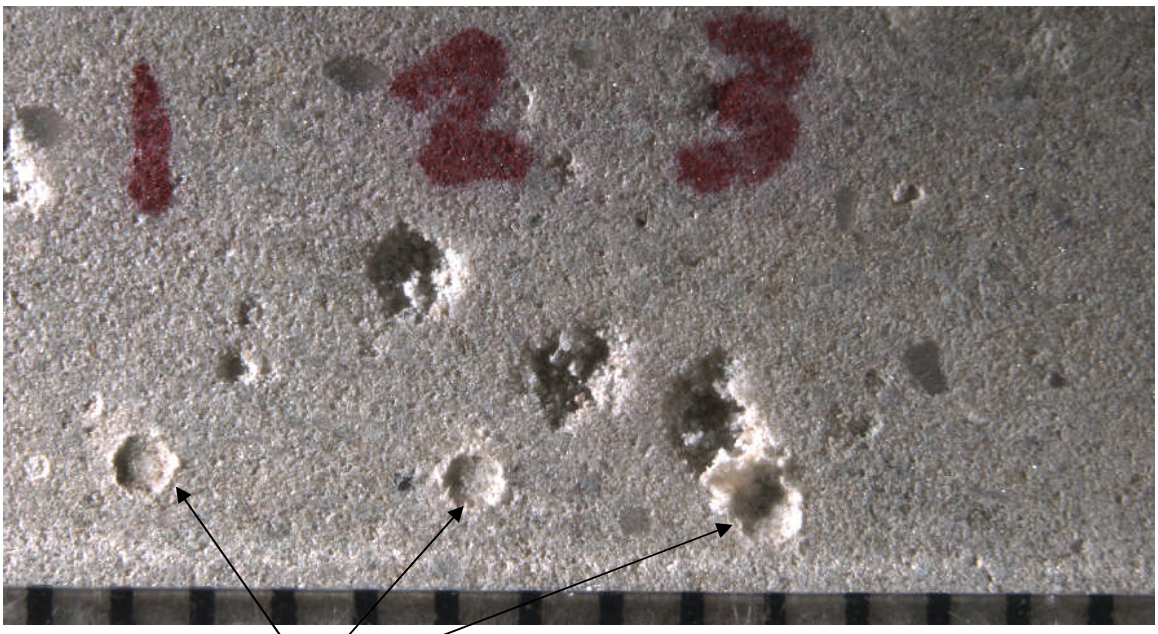

Indentation marks